International Journal of Heat and Mass Transfer 172 (2021) 121176

Contents lists available at ScienceDirect

International Journal of Heat and Mass Transfer

journal homepage: www.elsevier.com/locate/hmt

Experimental investigation of subcooled flow boiling in annuli with reference to thermal management of ultra-fast electric vehicle charging cables

V.S. Devahdhanush[a], Seunghyun Lee[a,b], Issam Mudawar[a,*]

[a] Boiling and Two-Phase Flow Laboratory (PU-BTPFL), School of Mechanical Engineering, Purdue University, 585 Purdue Mall, West Lafayette, IN 47907, USA
[b] Gwangju Institute of Science and Technology Two-Phase Flow and Thermal Engineering Laboratory, School of Mechanical Engineering, 123 Cheomdangwagi-ro, Buk-gu, Gwangju 61005, South Korea

ARTICLE INFO

Article history:
Received 22 December 2020
Revised 10 February 2021
Accepted 28 February 2021
Available online 25 March 2021

Keywords:
Subcooled flow boiling
Annulus
Electric vehicles
Charging system
Thermal management
Two-phase heat transfer coefficient

ABSTRACT

Transportation industry is presently in fast track to transition from Internal Combustion Engine Vehicles (ICEVs) to Electrical Vehicles (EVs). One of the most pressing challenges to full adoption of EVs is very slow charging at the networks of charging stations proposed worldwide. Despite many recent so-called 'ultra-fast' charging methods, which capitalize on a variety of single-phase liquid schemes to cool the charging cable, thermal constraints limit the electrical current carrying capacity of the fastest commercial chargers to about 500 A. Achieving the faster charging time required for the anticipated proliferation of EVs will require increasing this current capacity to at least 2000 A, which poses formidable thermal challenges in design of the charging cable. This study explores the development of a vastly more powerful charging cable thermal management scheme to achieve this higher current threshold. Subcooled flow boiling is proposed as the primary means to dissipating the larger amounts of heat generated at higher currents. Experiments are performed by pumping highly subcooled dielectric liquid HFE-7100 though a concentric circular annulus mimicking a segment of an actual cable, with a uniformly heated 6.35-mm-diameter inner surface representing the electrical conductor and adiabatic 23.62-mm-diameter outer surface the external conduit. All experimental cases considered are conFig.d to ensure subcooled fluid conditions throughout the test module. It is shown the proposed cooling scheme is capable of tackling currents up to 2438 A, around four times higher than the present-day commercial maximum. With appropriate batteries and other ancillary components, this technology is expected to bring EV charging times down to less than 5 minutes. Aside from demonstrating this potential, an assessment of available subcooled boiling heat transfer coefficient correlations identified Moles and Shaw's to predict the new experimental data with an overall mean absolute error of only 11.68%. The flow and heat transfer physics are also explained in detail.

1. Introduction

1.1. Electric vehicle trends

Electric Vehicle (EV) usage has been steadily on the rise in the transportation sector because of numerous inherent benefits over petroleum-oil-based vehicles/Internal Combustion Engine Vehicles (ICEVs) [1,2]. Some advantages include reduced overall pollution [3–5], negligible emission from EVs resulting in better air quality, especially in cities and high traffic areas, and both lower cost [6] and noise [7] of operation, all due to the absence of internal combustion engines. Another reason for migration away from petroleum-based vehicles is the rapid depletion of crude oil worldwide. The U.S. Energy Information Administration has suggested that there would be adequate supply of crude oil and other liquid hydrocarbons through 2050, however there is uncertainty in both price and demand from different parts of the world [1,8]. The International Energy Outlook 2019 estimates a substantial increase in electricity and natural gas consumption and a small increase in jet fuel consumption for transportation worldwide by 2050 [8]. Other reasons for the increase in EV usage are falling prices, vast research and development efforts, and overall environmental benefits, especially when the electricity used for EVs is generated from renewable sources. The global EV market is expected to grow by at least a factor of ten by 2025 [2].

* Corresponding author.
E-mail address: mudawar@ecn.purdue.edu (I. Mudawar).
URL: https://engineering.purdue.edu/BTPFL (I. Mudawar)

https://doi.org/10.1016/j.ijheatmasstransfer.2021.121176
0017-9310/

Nomenclature

A	area
A_c	cross-sectional area
Bo	boiling number, $Bo = q''_s/Gh_{fg}$
C	empirical coefficient
c_p	specific heat at constant pressure
D	diameter
D_e	equivalent diameter
D_h	hydraulic diameter
D_{hp}	diameter based on heated perimeter
E	enhancement factor
Fr	Froude number
G	mass velocity
g	gravitational acceleration
h	enthalpy; heat transfer coefficient
$\bar{h}$	average heat transfer coefficient
h_{fg}	latent heat of vaporization
I_{wire}	current through charging wire
Ja^{**}	modified Jakob number, $Ja^{**} = c_{p,f}\Delta T_{sub}/h_{fg}$
k	thermal conductivity
L	length
m	empirical constant
$\dot{m}$	mass flow rate through annulus
M_W	molecular weight
Nu	Nusselt number
N	number of datapoints
P	pressure
P_F	friction perimeter
P_H	heated perimeter
P_R	reduced pressure
Pe	Peclet number
Pr	Prandtl number
Q_v	volumetric flow rate
q	heat rate
q''	heat flux
r^*	radius ratio, $r^* = D_i/D_o$
R	electrical resistance
Re	Reynolds number
S	safety factor; suppression factor
T	temperature
$\bar{T}$	average temperature
ΔT_{sat}	surface superheat, $\Delta T_{sat} = T_s - T_{sat}$
ΔT_{sub}	fluid subcooling, $\Delta T_{sub} = T_{sat} - T_f$
t	time
U	bulk fluid velocity
x_e	thermodynamic equilibrium quality
z	axial coordinate

Greek symbols

α	void fraction; temperature coefficient of wire
μ	dynamic viscosity
ν	kinematic viscosity
ψ	dimensionless heat transfer rate
ψ_0	dimensionless heat transfer rate corresponding to $x_e = 0$
ρ	density; electrical resistivity of wire
σ	surface tension
θ	percentage predicted within ±30%
ξ	percentage predicted within ±50%

Subscripts

exp	experimental
f	liquid; bulk fluid
g	vapor
h	heated
H	heater
i	inner tube of annulus
in	channel inlet
nb	nucleate boiling
o	outer tube of annulus
out	channel outlet
pred	predicted
s	surface
sat	saturation
sc	subcooled boiling
sp	single-phase
tc	thermocouple
z	local (along axial direction)

Acronyms

AC	Alternating Current
AWG	American Wire Gauge
CHF	Critical Heat Flux
DC	Direct Current
DNB	Departure from Nucleate Boiling
EV	Electric Vehicle
EVSE	Electric Vehicle Supply Equipment
FDB	Fully Developed Boiling
ICEV	Internal Combustion Engine Vehicle
MAE	Mean Absolute Error (%)
ONB	Onset of Nucleate Boiling
PDB	Partially Developed Boiling
PHEV	Plug-in Hybrid Electric Vehicle
RTD	Resistance Temperature Detector

Still, there are numerous obstacles that stand in the way of worldwide EV proliferation. These include: (i) the energy storage capacity of batteries is smaller than that of gasoline tanks in ICEVs of similar specifications [9], (ii) the average time required to charge an EV battery is much longer than the re-fueling time for petroleum-based vehicles, (iii) building a wide network of charging stations is not a trivial task and requires a massive investment upfront, (iv) the existing electrical grids might not be able to cater to the increased power demands for these charging stations, and lastly, (v) the upfront 'technology cost' is still too high to attract the average consumer.

This study is concerned entirely with the charging of EVs. And, for the purposes of this study, the phrase 'electric vehicles' also encompasses Plug-in Hybrid Electric Vehicles (PHEVs).

1.2. Charging of electric vehicles

1.2.1. EV charging systems

Electric vehicle charging systems, also called Electric Vehicle Supply Equipment (EVSE), can be classified into Alternating Current (AC) or Direct Current (DC) based on the location where AC-to-DC conversion takes place. AC-DC conversion is necessary because power is transmitted through the electrical grid as AC but is stored in batteries as DC. In typical AC charging, conversion takes place on-board the EV, whereas in typical DC charging, this takes place at the ground station. AC charging enables EV manufacturers to completely design their conversion systems and other components based on battery specifications and other factors, and thereby control most of the charging operation. DC charging systems have fewer components on-board the EVs themselves and therefore reduce the onboard space and weight, but additional standards are available for manufacturers to maintain uniformity [10]. DC chargers are usually faster than their AC counterparts. The

Table 1
EV charging levels in North America, Europe, and China.

Charging Level/Mode	Nominal Supply Voltage (V)	Maximum Continuous Current (A)
North America (SAE J1772) [11]		
AC Level 1	120 VAC, 1-phase	12 A, 16 A
AC Level 2	208-240 VAC, 1-phase	80 A
AC Level 3 (not implemented)	208-240 VAC, 1-phase	400 A
DC Level 1	50-1000 VDC	80 A
DC Level 2	50-1000 VDC	400 A
Europe (IEC 61851-1, 61851-23) [12,13]		
Mode 1 (AC)	250 VAC max., 1-phase; 480 VAC max., 3-phase	16 A
Mode 2 (AC)	250 VAC max., 1-phase; 480 VAC max., 3-phase	32 A
Mode 3 (AC)		>32 A, in accordance with connector used
Mode 4 (DC)	18-1500 VDC (500 VDC max. for configuration AA)	300 A
Mode 4 (DC Combined Charging System) [13]	1000 VDC max. (500 VDC max. for configurations CC, DD, EE and 1000 VDC max. for FF)	In accordance with connector used
China (GB/T 20234.1, 20234.2, 20234.3, 18487.1) [14–17]		
Mode 1 (AC)	Prohibited	
Mode 2 (AC)	220 VAC 1-phase, 250 VAC max.	8 A, 13 A
Mode 3 (AC)	220 VAC 1-phase, 380 VAC 3-phase, 440 VAC max.	32 A (1-phase; Case A, B, or C connections), 63 A (3-phase; Case C connection)
Mode 4 (DC)	1000 VDC max., >1000 VDC upon consultation	250 A preferred max., 400 A max. (Only Case C connection)

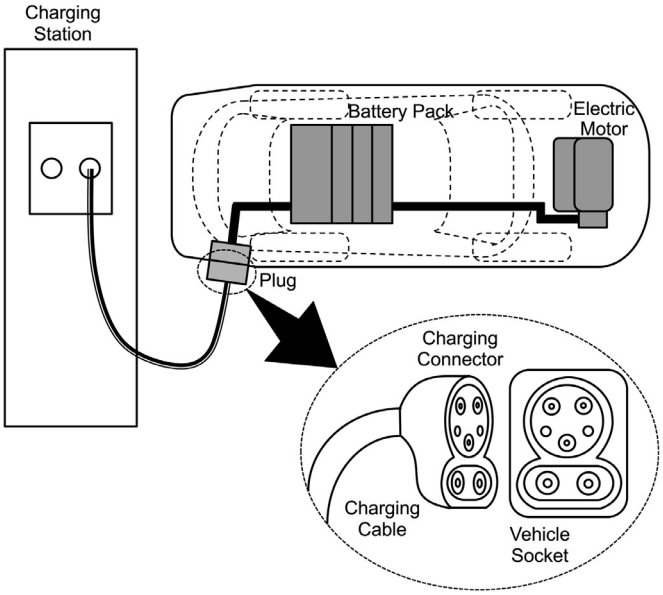

Fig. 1. Key components of a typical DC electric vehicle charging system. Combined Charging System Type 1 standard (J1772 AC + CCS) connector is shown as an example.

key components of a typical DC electric vehicle charging system are illustrated in Fig. 1. Power is supplied from the charging station through a long charging cable, which terminates in a standardized connector plug. This mates with a corresponding socket on the EV. On-board the EVs, power is stored in a high-capacity battery pack and is supplied to the electric motor as needed.

A summary of EV charging levels/modes worldwide [11–17] is given in Table 1. Listed are categories in North America, Europe, and China, directly taken from the corresponding standards (latest as of December 2019). Charging systems can be categorized into three based on their charging power levels: Level 1 (Opportunity), Level 2 (Primary), and Level 3 (Fast) [11,18,19]. Typically, AC Level 1 and AC Level 2 chargers do not need prior authorization from utility providers because of their low power consumption, but the other types do [19]. Numerous standards of EV chargers, such as J1772, CHAdeMO, GB/T, Mennekes, and Tesla, are popular in today's market. Knez *et al.* [20] have enumerated the strengths and weaknesses of each of these types. The most common charger standards in the USA, the European Union, and China are J1772, Mennekes, and GB/T, respectively [20]. All EVSE connector standards have been summarized by Das *et al.* [19] along with pictures of the most commonly used connectors. Fig. 1 shows the Combined Charging System (CCS) Type 1 (based on J1772) connector as an example. The bottom two ports of the connector carry DC current, while the top is for AC and communication signals.

1.2.2. Review of today's fastest EV chargers

Some of the fastest EV chargers available in market today are listed in Table 2. It is to be noted that, with the EV charging industry being relatively new, there are a lot of startups, acquisitions, mergers, brand changes, *etc*., and with vast research and development currently happening, it is difficult to quote all the products. In 2017, Meintz *et al.* [21] suggested that charging speed needed to be increased from the then-maximum of 120 kW to at least 400 kW to make EV charging times even comparable to conventional gasoline fueling times. From Table 2, it is clear that the fastest EV charger available today is 500 kW. Comparing this to the effective charging rate of a light passenger ICEV – 5000 kW including all losses [9,22] – today's fastest EV charging occurs at a rate that is an order of magnitude slower.

1.2.3. Behavioral and ancillary factors influencing EV charging

The charging behavior of EV owners is a big factor in developing EV charging infrastructure. With the presently available infrastructure, most EV owners charge their vehicles primarily at their homes, followed by their workplaces, and then public charging stations [23]. There is no quantifiable role of public fast charging in literature because of their present speed, and that consumers might have been using them for their 'free' promotions in their early stages of installation than for actual driving [23,24]. This behavior might change if the charging times at public fast charging stations become as short as ICEV fueling times. EV owners may have difficulties in the compatibilities of their vehicles and the presently available charging infrastructure [23]. Another interesting statistic is that EV users typically often charge their vehicles in a timely manner, whereas most ICEV users refuel their tanks when they get near empty [25]. But this could be because of the current infrastructure. The cost of fast charging also plays a factor in making the decision [26,27]; if the demand for fast charging increases, the average cost would come down, which would in turn attract more people to use this option.

Table 2
Existing fast(est) EV chargers around the world.

Charger	Maximum Charging Rate	Cooling Scheme
Tesla Supercharger V2 [w1]	480 VDC, 120-145 kW	Natural convection air cooled cables
Tesla Supercharger V3 [w1]	480 VDC, 250 kW	Liquid cooled
ITT Cannon CCS1 and CCS2 [w2]	1000 VDC, 500 A	Dielectric liquid cooled cable, connector, and contacts
Huber+Suhner Radox HPC [w3]	1000 VDC, 500 A	Active liquid cooling system of connector and cable
Tritium Veefil-PK [w4]	950 VDC, 350 kW	Active liquid cooling of entire user unit
ABB Terra HP (Used by Ionity and EVgo) [w5,w6,w7]	350 kW, 920 VDC	Liquid cooled cables
BTC Power 350kW HP DCFC [w8]	950 VDC, 350 kW (432 A max. up to 920 VDC, 500 A max. up to 500 VDC)	
Efacec HV350 [w9]	920 VDC, 322 kW, 350 A (500 A max. up to 640 V)	
ChargePoint Express Plus [w10]	500 kW, 1000 VDC, 500 A	Liquid cooled electrical module and cables
Siemens 150kW high power [w11]	150 kW, 920 VDC	
Tellus Power DC 150 Charger [w13]	187 kW, 250 A, 750 V	Active air cooled
DBT Dispenser HPC [w14]	350 kW, 1000 VDC	Liquid cooled cable >200 A
Endesa X Ultra-fast pantograph [w15]	500 kW	
Circontrol Raption 150 CCS [w16]	150 kW, 920 VDC, 200 A	Forced air cooled unit
Phihong DO 360 CCS1 [w17]	360 kW, 950 VDC, (379 A @ 950 V, 500 A @ 720 V)	Liquid/fan cooled unit
FreeWire Boost Charger [w18]	120 kW, 500 VDC	

Dixon *et al.* [9] suggested that EV usage does not come with a charging time penalty if the range of travel is shorter than the EV's battery storage capacity since the battery can be charged at home or at workplace/destination where it is parked over a long period of time provided there is infrastructure for doing so. For longer travel distances, there are negligible travel delays if the drivers take appropriate breaks in their journey and if there are charging stations whenever needed. But on the other hand, for continuous driving, charging on-route means delays which are directly related to the charging rate and battery size.

1.2.4. Limitations to speed of charging

The speed of charging is mainly limited by the thermal limitations of the charging system and battery, and the capacity of the battery. With the capacity of the battery being mostly constant, faster charging times typically mean the transfer of a larger amount of energy in a shorter duration. Ultra-fast (extreme-fast) charging schemes can be implemented either by increasing the charging voltage or current. Increasing the charging voltage comes with the challenges of cybersecurity and safety risks, costly and bulky EV thermal design, development of new connectors, battery, power electronics, non-standard chargers, *etc.* [21]. The major challenge to increasing the charging current is designing high current cables and connectors that can tackle the vast amounts of heat generated.

One of the main concerns with and a barrier to large-current ultra-fast charging is the large amount of heat generated within the charging cable because of the high amperage current flowing through it. Most charging cables use conventional air cooling to remove this generated heat. Some researchers have proposed active liquid cooling of charging cables to remove larger amounts of generated heat and thereby have a larger amperage of current flowing through them [28,29]. Others have also proposed active liquid cooling of electrical connections [30]. Overall, this study is focused on the thermal management of high-amperage ultra-fast charging cables.

1.3. Thermal management of EV chargers

Table 2 makes it apparent that there has been a shift in the cooling scheme used for today's fastest chargers from forced air cooling towards active liquid cooling owing to superior thermophysical properties of the latter. But even with active liquid cooling, the maximum continuous current through charging cables is ~500 A. This low cooling performance is a major disadvantage of single-phase liquid cooling schemes. Two-phase cooling schemes, on the other hand, typically capitalize on both the coolant's sensible and latent heat to greatly enhance the heat transfer performance and help maintain the cable at a much lower temperature than possible with single-phase cooling [31].

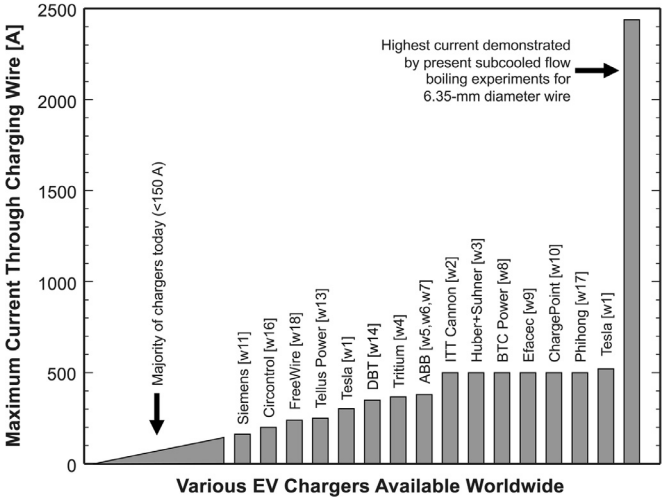

Fig. 2. Maximum continuous current through the charging wire of various EV chargers available worldwide. The highest possible current demonstrated by experiments in the present study is included as a reference.

Various two-phase cooling schemes have been investigated by researchers at the Purdue University Boiling and Two-Phase Flow Laboratory (PU-BTPFL) and other groups around the world. These include capillary-driven devices [32,33], pool boiling thermosyphons [34,35], falling films [36,37], channel flow boiling [38–43], jet impingement [44,45], sprays [46,47], and hybrids between different schemes [48]. This study is concerned entirely with subcooled flow boiling. The bar graph in Fig. 2 shows the maximum continuous current through charging wires of various EV chargers available worldwide. The majority of chargers supply a continuous current of less than 150 A, and some of the latest fast DC chargers ~520 A. The highest possible continuous current demonstrated by steady-state subcooled flow boiling experiments in the present study is included as a reference. This is almost four times higher than the present-day maximum.

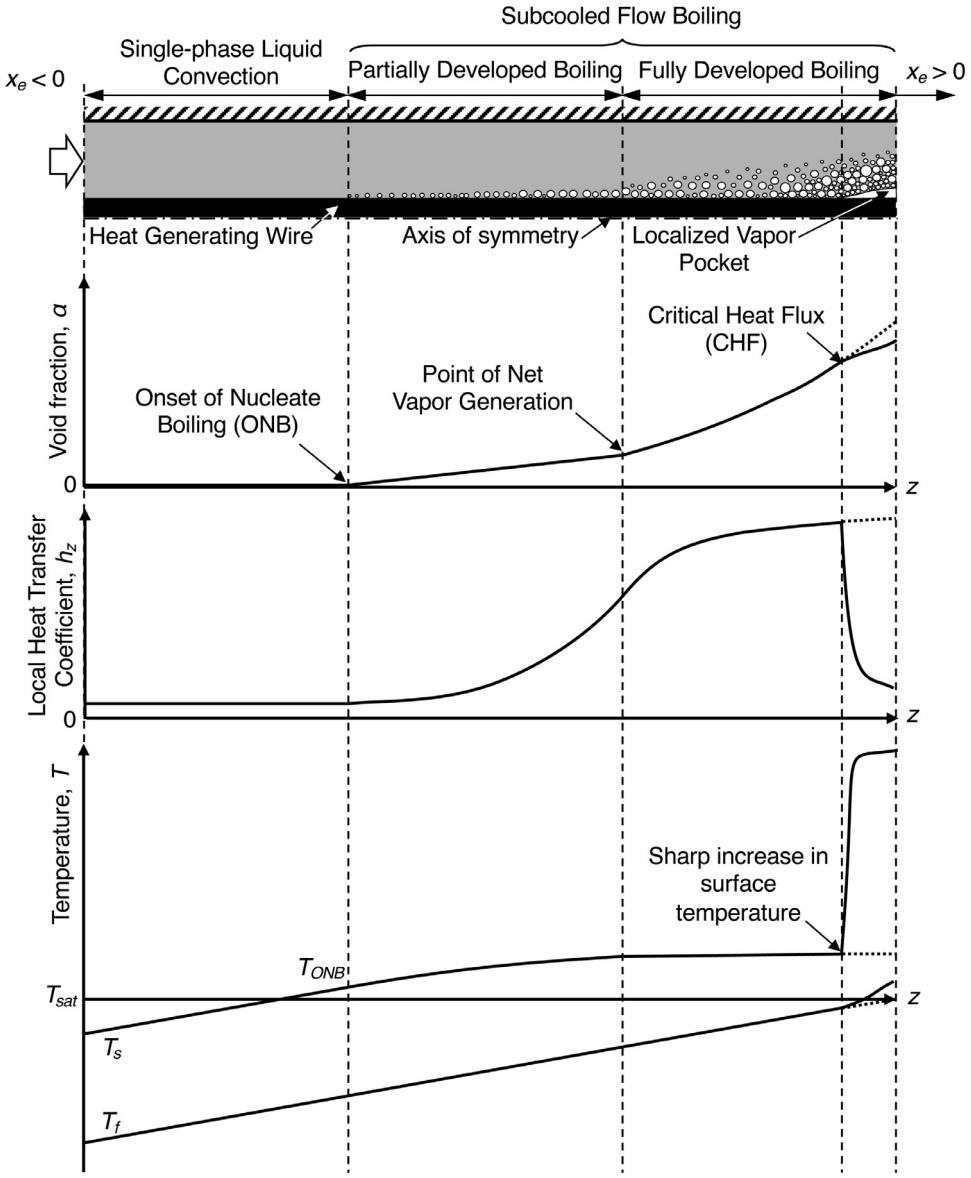

Fig. 3. Schematic representation of typical subcooled boiling flow with corresponding local void fraction, heat transfer coefficient, and temperature profiles.

1.4. Subcooled flow boiling

Depending on the state of fluid introduced into the cooling device, flow boiling can occur in either subcooled or saturated states. If the flow channel is long enough, there is a possibility of transitioning from subcooled to saturated boiling. The entrant liquid is said to be in a subcooled state if it is at a temperature lower than its saturation temperature at the operating pressure. Most cooling applications utilize subcooled inlet conditions. Subcooled flow boiling is also proposed in this study, as a means to cool down high-current charging cables. Subcooled flow boiling capitalizes on both the sensible and latent heat of the fluid to yield better cooling performance and a higher Critical Heat Flux (CHF) than saturated boiling. Some methods of sustaining subcooled flow boiling along the entire channel length are by increasing flow rate, inlet liquid subcooling, or diameter [40]. Subcooled flow boiling in conventional channels [49,50] and annuli [43,50–54] has been studied for many decades.

1.4.1. Flow and heat transfer physics

Fig. 3 is a schematic representation of typical subcooled boiling flow in an annulus with corresponding local void fraction, heat transfer coefficient, and temperature profiles. Shown is an axisymmetric section of the annulus around the axis of symmetry. The bottom of the top schematic represents the axis of symmetry at the center of a heat generating wire and the top wall an outer adiabatic sheath. Ignoring material property variations with temperature, the heat flux from the inner surface is considered uniform. Fluid enters the annulus in a subcooled liquid state, gains sensible heat from the inner surface by forced convection and increases in temperature. Entrance effects are not illustrated but would be present near the liquid inlet. The void fraction remains constant at zero in the absence of any vapor production. . The heat transfer coefficient for single-phase forced convection remains fairly constant (excepting the short upstream developing boundary layer region) and both the mean liquid temperature and surface temperature increase axially is an almost linear fashion. At a location downstream, the inner surface temperature begins to exceed the temperature required for Onset of Nucleate Boiling (ONB) and the first

bubbles nucleate with the bulk fluid remaining subcooled. Both void fraction and heat transfer coefficient start increasing with the latter at a much higher rate because of the considerable contribution of latent heat transfer. As a result, the slope of surface temperature decreases with the bulk fluid temperature still increasing in a manner fairly similar to that in the upstream single-phase regime. The upstream subcooled boiling regime is termed Partially Developed Boiling (PDB) or Highly Subcooled Boiling [55]. It is characterized by nucleating bubbles collapsing or sliding along the heated surface with negligible growth because of strong condensation effects. Appreciable condensation also causes the void fraction to increase at a very small rate. Bubbles of different sizes are produced in this regime with the bubbles downstream typically larger because of the higher superheat available for nucleation. Coalescence of nearby bubbles may be seen resulting in bigger or oblong bubbles. At the point of net vapor generation, bubbles begin lifting off from the surface and the flow transitions to Fully Developed Boiling (FDB) or Slightly Subcooled Boiling. Void fraction now increases at a much higher rate than in PDB because of the departing bubbles drawing fresh liquid to contact the surface, a higher rate of bubble production, and weaker condensation effects near the surface with the bulk fluid being hotter. The local heat transfer coefficient increases at a slower rate and plateaus downstream in this regime at a value higher than that of the upstream single-phase liquid heat transfer coefficient typically by an order or more in magnitude. The surface temperature in FDB increases at a very slow rate with the bulk fluid temperature still increasing in a fairly linear fashion. The schematic also portrays the development of a bubble boundary layer and bubbles getting smaller after lift-off because of condensation by the cooler bulk liquid. In the latter part of FDB, the bubbles may be very large and irregularly shaped, and occupy an appreciable part of the channel at high heat fluxes and low pressures [55]. FDB extends to the point at which thermodynamic equilibrium quality, x_e, reaches zero value, which signals commencement of the Saturated Boiling regime. It is emphasized that lengths of single-phase, PDB, and FDB regimes can vary greatly from one another compared to how they are depicted in Fig. 3.

The above-mentioned advantages of phase change, namely very high heat dissipation rate and fairly constant surface temperature, are available only in the nucleate boiling flow regime, which is limited by CHF. At CHF, flow transitions to film boiling and is accompanied by an unsteady and uncontrollable rise in surface temperature. CHF in subcooled boiling is typically the result of localized vapor blankets forming along the heated surface even where bulk liquid is quite abundant. Whereas CHF in saturated boiling is the result of gradual thinning and eventual dryout of an annular liquid film at the heated surface caused mostly by liquid deficiency [40]. CHF may or may not occur in the subcooled boiling, and the location at which it occurs depends on operating conditions. Shown in Fig. 3 is an example of a localized vapor blanket at the very downstream location of the annulus. A massive coalesce between bubbles may trigger the formation a large vapor blanket and a Departure from Nucleate Boiling (DNB). After CHF, the surface temperature increases rapidly to dangerous levels because of the low thermal conductivity of vapor and therefore a smaller amount of heat being conducted and radiated to the liquid-vapor interface where the phase change takes place. As a result, the heat transfer coefficient nosedives and the bulk fluid temperature increases at a higher rate because of the much hotter surface.

1.4.2. Demarcation between flow regimes

Onset of nucleate boiling has been analytically investigated by many researchers [49,56–60]. Hsu and Graham [57] postulated that, for a bubble to nucleate from a cavity, the superheat of the liquid layer near the nucleation cavity must be greater than that required for the bubble to grow beyond the cavity. Good agreement of this model with experimental data for water, pentane, and ether was shown later [58]. Bowring [56] suggested that ONB corresponds to the point of intersection of the pure single-phase and subcooled boiling curves. Sato and Matsumura [59] later developed an analytical model that does not require contact angle or thermal layer thickness information.

Flow regime transition from PDB to FDB has also been investigated by many researchers [49,56,61–63]. Bowring [56] proposed a dimensional correlation to predict the point of net vapor generation, and proposed that the net heat flux throughout PDB is the sum of heat fluxes associated with single-phase convection and bubble nucleation. This type of superposition is similar to one proposed by Rohsenow [61] but the expressions used for the single-phase component are different [55]. Bowring also suggested that the transition occurs at the point of intersection of the actual boiling curve (plotted from subcooled flow boiling experiments) and the subcooled pool boiling curve [56].

Bergles and Rohsenow [49] presented a slightly different model with a similar intersection point of transition but a different method of superposition in the PDB regime. Shah [62] used dimensionless parameters and presented fully empirical transition criteria based on a large database including several fluids. Recently, Shah [64] suggested using the simple criterion for point of net vapor generation proposed earlier by Saha and Zuber [63], which is based on the premise that at lower and higher flow rates, bubble detachment is thermally controlled, occurring at a fixed Nusselt number, and hydrodynamically controlled, occurring at a fixed Stanton number, respectively. Dorra *et al.* [65] reviewed several predictive models for the onset of significant void in subcooled boiling and also recommend using the Saha and Zuber criterion.

1.4.3. Annulus flow geometry

Most studies in the literature deal with circular or rectangular channel flows with heating from some or all surfaces. Concentric annular channels, although an important geometry used in applications such as double-pipe heat exchangers, have received lesser attention. Owing to the presence of two heat transfer surfaces, there is a wider variety of thermal boundary conditions for flows in annuli. Table 3 lists all four fundamental thermal boundary conditions for flow in an annulus [66,67]. Solutions to any other thermal boundary condition can be found from these fundamental solutions using interpolation techniques.

One important parameter commonly used to characterize flow in concentric annular channels is radius ratio, r^* [67]. As will be discussed later, different studies have employed different equivalent diameters, such as hydraulic diameter based on friction perimeter, hydraulic diameter based on heated perimeter, laminar equivalent diameter, heated diameter, *etc*.

1.5. Objectives of study

The present study investigates application of subcooled flow boiling as a thermal management solution for ultra-fast EV charging cables. The study will detail the experimental methods used to investigate subcooled flow boiling through an internally heated annulus. A preliminary analysis is provided to explore the effects of various parameters on heat transfer performance and help arrive at a baseline design of the charger cooling system. An experimental facility is constructed with a test module similar to a section of the charging cable and cooling conduit assembly. A custom-built heater is used to mimic heat generation due to high current flow though the charging wire. Various test cases are systematically conducted to explore the performance of the proposed cooling system. The heat transfer physics within the test module

Table 3
Fundamental thermal boundary conditions for annular flow.

	Tube-1	Tube-2
First kind	Uniform temperature	Uniform temperature (equal to inlet fluid temperature)
Second kind	Uniform heat flux	Adiabatic (well insulated)
Third kind	Uniform temperature	Adiabatic (well insulated)
Fourth kind	Uniform heat flux	Uniform temperature (equal to inlet fluid temperature)

are explained for various operating conditions. The collected datapoints are demarcated into their respective flow regimes which are represented in flow regime contour maps. The predictive performance of various existing subcooled boiling correlations is assessed.

With appropriate batteries and other ancillary components, this thermal management technology is expected to bring EV charging times down to less than 5 minutes, about the time required for conventional gasoline filling [9]. This technology can also be utilized for cooling high current electrical wires in other applications.

2. Experimental methods

2.1. Two-phase flow loop

Fig. 4(a) shows a schematic diagram of the two-phase flow loop used in the present study and Fig. 4(b) provides a photograph of the experimental facility with key components identified. HFE-7100, a dielectric heat transfer fluid, is used as coolant in this closed loop, a major portion of which is stored in a liquid reservoir. Liquid is pumped from the reservoir by a Fluid-o-Tech internal gear pump situated at the lowest level of the facility to help prime the flow lines and increase gravitational head at the pump inlet to avoid cavitation. The pump is magnetically coupled to an AC totally-enclosed-fan-cooled motor mounted on vibration dampeners and powered by a variable frequency drive to adjust the flow rate. A Swagelok relief valve is installed at the pump outlet, where loop pressure is highest, and is calibrated to crack open at 50 psig. Fluid from the pump passes through a FlowEzy stainless-steel industrial process filter that helps remove possible impurities in the fluid. Flow can be routed to one of two Omega FL rotameter flow meters within each flow rate is indicated by position of a stainless-steel float. A main flow control valve (Swagelok, C_v =1.80) downstream of the rotameters is used to adjust flow resistance in the loop, thereby regulating both pressure and flow rate, and helping prevent pressure oscillations with the test module. Fluid is then subcooled by flowing through a SWEP plate-type heat exchanger with 10 stainless-steel plates, rejecting heat to a counter flow of water circulated with the aid of a Lytron MCS50 modular cooling system. The fluid enters the test module in a subcooled state and gains both sensible and latent heat as it passes through the module. Depending on operating conditions, the fluid exiting the module may be in pure liquid or liquid-vapor mixture states. To condense any vapor and bring the fluid to desired reservoir temperature, the fluid is passed through a SWEP plate-type heat exchanger with 20 plates, in a vertical downward orientation for best condensing performance. A counter flow of distilled water is circulated through the other flow side of the heat exchanger with the aid a Lytron MCS20 modular cooling system. Exiting the heat exchanger, the liquid is returned to the reservoir, which is fitted with inlet and outlet valves to help maintain constant pressure during experiments. It should be mentioned that both of the system's Lytron water loops contain their own filters and flow control valves. Additionally, plug valves are present at multiple points of the flow loop for added bypass and flow control purposes.

A degassing system is present upstream of the gear pump in parallel with the main flow line to remove dissolved non-condensable gases like air from the working fluid and ensure accuracy of experimental data. It consists of a 3M Liqui-cel degassing contactor through which the working fluid flows at low flow rate, and is connected to a GAST oil-less diaphragm vacuum pump to apply vacuum on the other side of the degassing membrane. Degassing is done before experimentation and at regular intervals thereafter.

Table 4
Key dimensions of module.

Heated length, L_h	304.8 mm
Outer diameter, D_o	23.62 mm
Inner diameter, D_i	6.35 mm
Thermocouple locations from start of heated length, z_{tc}	25.4, 88.9, 152.4, 215.9, 279.4 mm

2.2. Test module

The main component of the test module is a custom-made very-high-power-density cartridge heater that is used to approximate heat dissipation from an AWG3 wire. Fig. 5(a) shows a longitudinal sectional diagram of the test module with key parameters indicated. The heater, having a diameter of $D_i = 6.35$ mm, is placed along the central axis of a stainless-steel tube of inner diameter $D_o = 23.62$ mm, with the fluid flowing through the annulus. The heated length of the heater of $L_h = 304.8$ mm starts 88.9 mm from the upstream end and is followed by another 165.1-mm unheated section. Key dimensions of the module along with thermocouple locations are given in Table 4. Note that the wire diameter is 6.35 mm, whereas the diameter of a standard AWG3 wire is 5.827 mm.

Fig. 5(b) shows a photograph of the module prior to complete assembly. Five type-T thermocouples are silver-soldered (using Brownells Silvaloy 355) to the Incoloy heated surface at several equidistant locations from the start of the heated length. Care is taken to isolate the two leads of all thermocouples from each other by application of Loctite high-temperature silicone adhesive to just before the junction. The heater is held at the exact center by fittings at its electrical-lead end. As shown in Fig. 5(c), the other heater end is held at the exact axial center using a 6.35-mm thick honeycomb core (Plascore PAMG) made of Aluminum alloy 5052. A perfect annular geometry and tight-fit are achieved by machining the honeycomb core using a computerized numerical control water-jet cutting machine. Aside from the heater positioning, the honeycomb mesh serves the important purpose of distributing flow streamlines uniformly about the annulus.

Variable power is supplied to the module heater using a 0-140 V, 1.4 kVA autotransformer. Forced convective air cooling is provided to the heater leads to prevent over-heating caused by the high amperage current flowing through. The entire module is mounted horizontally in the test facility and insulated with a 12.7-mm thick foam layer (Armacell AP/Armaflex) to prevent heat losses to the ambient.

2.3. Instrumentation and measurement accuracy

Fluid temperatures and pressures are monitored at the test module inlet, test module outlet, and liquid reservoir using

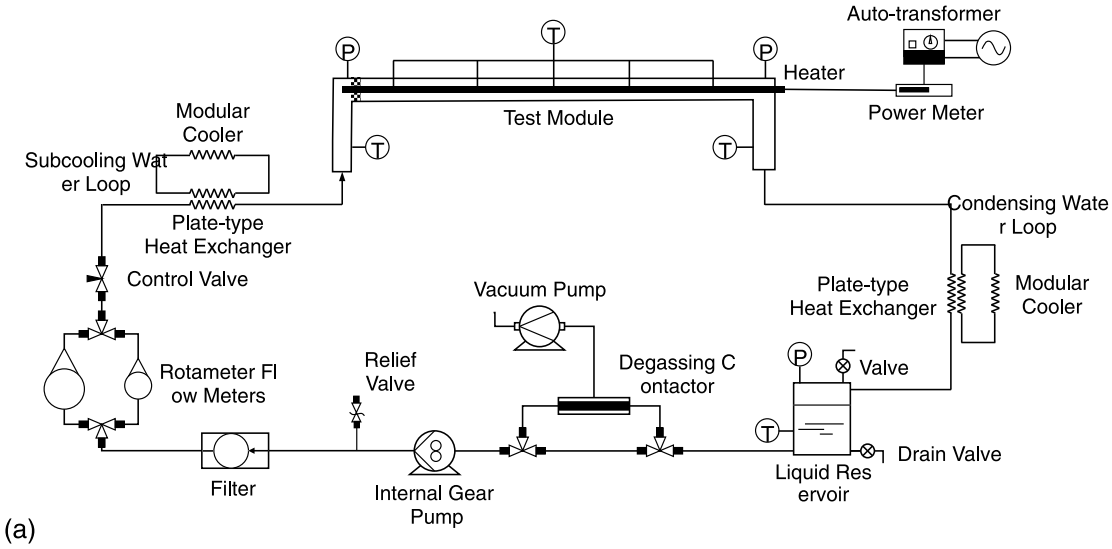

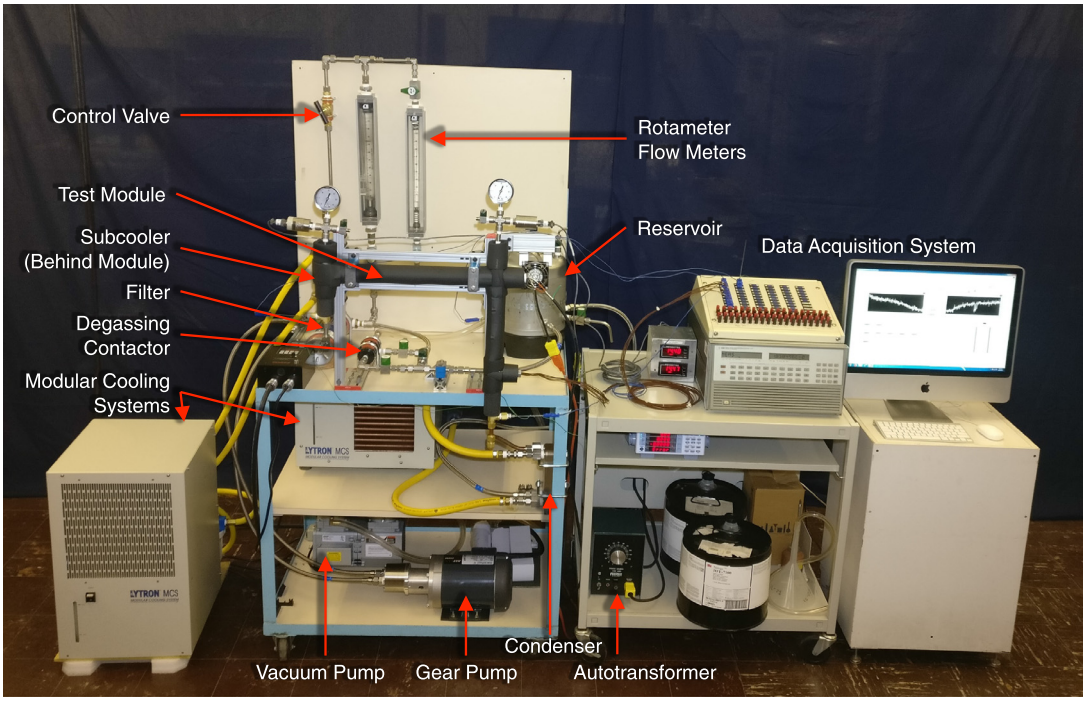

Fig. 4. (a) Schematic diagram of experimental two-phase flow loop. (b) Photograph of experimental facility with key components indicated.

sheathed type-T thermocouples and glycerin-filled analog pressure gauges. The module inlet and outlet pressures are also measured using Sensotec absolute pressure transducers.

All thermocouples used in the facility are calibrated over a range of -25 to 80°C against a standard platinum Resistance Temperature Detector (RTD) in a temperature controlled thermal bath. The RTD (Omega, Pt 100 1/10 DIN) has a mean accuracy of ±0.03°C and the Neslab RTE-220 thermal bath a set accuracy of 0.01°C. Deionized water is used as bath fluid for temperatures higher than 7.5°C and a 50-50% vol. mixture of ethylene glycol and water for lower temperatures. During the calibration, the tips of all the thermocouples and the RTD are bunched together in the bath and readings are taken every 2.5°C after reaching steady state. The European curve of std. Pt RTD (ITS-90, $\alpha = 0.00385\ \Omega/\Omega/°C$) is used to convert resistance outputs to temperatures. An average of the steady state readings is taken at each bath temperature and the thermocouple temperature outputs are correlated against the RTD output using a least squares regression method to yield third order polynomials. This in-house calibration improved the accuracy of the thermocouples to less than ±0.1°C. After attaching the thermocouples to the heater, a further check is done by comparing the calibrated thermocouple values to the RTD output at various bath temperatures in the calibration range.

A Yokogawa WT310E power meter is used between the heater and autotransformer to measure the voltage, current, and power input to the heater. All electronic signals from the facility are collected using an FET multiplexer and measured by an integrating voltmeter of an HP data acquisition system. The measured readings are monitored and recorded on a computer using LabVIEW software.

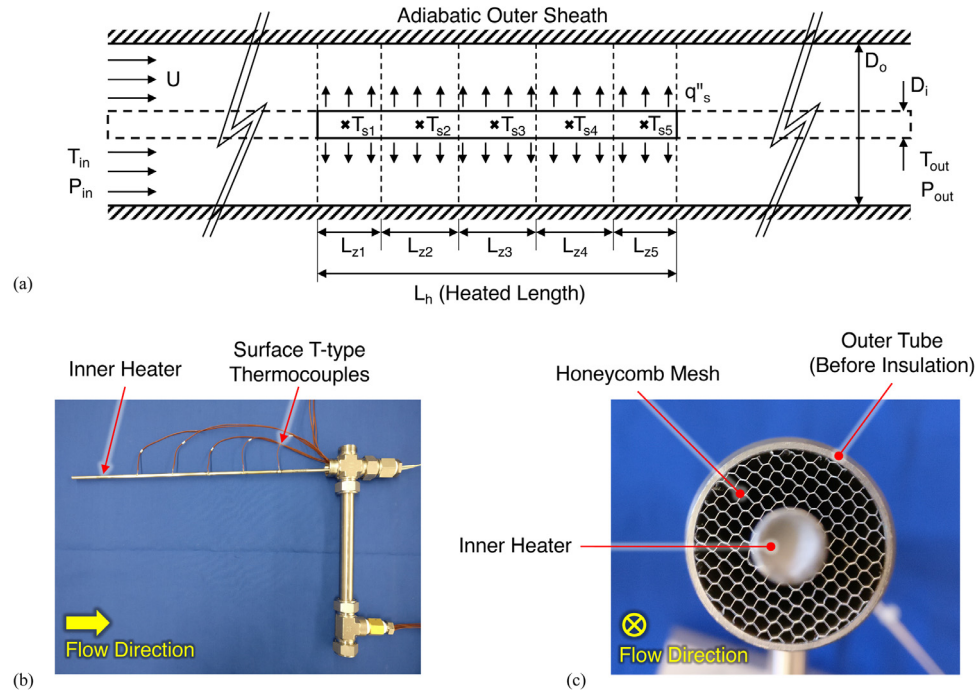

Fig. 5. (a) Schematic diagram of module. (b) Photograph of module before assembly. (c) Honeycomb core holding heater at exact center.

Maximum uncertainties in the measurements of temperature, absolute pressure, volumetric flow rate, and heater power are ±0.3°C, ±0.5%, ±2%, and ±0.85%, respectively.

2.4. Operating procedure

Prior to testing, all electronic sensors and the data acquisition system are turned on and the output signals are verified. Both the modular cooling systems supplying water to the condenser and inlet subcooler are also turned on. The reference pressure valve on the reservoir is opened to maintain a constant atmospheric pressure at this point of the closed loop. The main flow control valve is fully opened, and the degassing contactor isolated. Flow is routed through one of the rotameter flow meters depending on the desired flow rate value for a given test. The pump is turned on and the motor speed adjusted to set the required flow rate using a variable frequency drive. The autotransformer is powered up with the dial set at 0 V, corresponding to adiabatic flow through the test module. Once the flow becomes steady, the heaters are powered up to desired value by adjusting the autotransformer brush position. The system is carefully monitored for at least 30 minutes or until it reaches steady-state, and the data are recorded. This process is repeated following equal heat flux increments until the maximum design value or critical heat flux are reached. The entire test procedure is repeated for several flow rates.

2.5. Data processing

The flow configuration in this study is annular with a diabatic inner boundary and an adiabatic outer boundary. As explained below, the equivalent diameter for flow through an annulus is given by the relation

$$D_e = \begin{cases} D_h = \dfrac{4A_{ch}}{P_F}, \text{ if annular gap} > 4\text{mm} \\ D_{hp} = \dfrac{4A_{ch}}{P_H}, \text{ if annular gap} \le 4\text{mm} \end{cases}, \tag{1}$$

where

$$\text{annular gap} = \frac{D_o - D_i}{2}. \tag{2}$$

While both gap ranges use the same annular flow area, A_{ch}, annuli with larger gaps are characterized by hydraulic diameter, D_h, determined using the flow frictional perimeter, P_F, and those with smaller gaps are characterized by a special definition based on heated perimeter, P_H [62,68,69]. Some studies recommend a different annular gap transition point of 3 mm [64], while some suggest $D_e = D_{hp}$ for all annular gaps [70,71]. And most single-phase annular flow studies use D_h [67]. Based on all these recommendations, with an annular gap of 8.64 mm, the annular geometry in the present study is characterized using $D_e = D_h$.

The resistivity of a material is given by

$$\rho|_T = S\rho_{20^\circ C}(1 + \alpha\Delta T) = S\rho_{20^\circ C}(1 + \alpha(T - T_{20^\circ C})), \tag{3}$$

where $\rho_{20^\circ C}$ is resistivity at 20°C, α temperature coefficient, and S a safety factor determined by consideration of temperature distribution in the conductor leading to an increase in heat generation. For copper, $\rho_{20^\circ C} = 1.724 \times 10^{-8}$ Ωm and $\alpha = 4.29 \times 10^{-3}$ K^{-1}. S is considered to be unity for this study. The resistance of a wire can be calculated from Pouillet's law,

$$R = \frac{\rho L_{wire}}{A_{c,wire}}, \tag{4}$$

where L_{wire} and $A_{c,wire}$ are the length and cross-sectional area of the wire, respectively. Heat generation from a section of the wire is then given by $q_{wire} = I^2_{wire}R$, from which the heat flux dissipating from the surface of the wire (after setting $S = 1$) is determined using the relation

$$q''_s = \begin{cases} \dfrac{I^2_{wire}\rho_{20^\circ C}(1 + \alpha(T_s - 20^\circ C))}{(\pi^2/4)D^3_{wire}} & , T_s \ge 20^\circ C \\ \dfrac{I^2_{wire}\rho_{20^\circ C}}{(\pi^2/4)D^3_{wire}} & , T_s < 20^\circ C \end{cases}. \tag{5}$$

Equation (5) is adopted in this study to determine the heat flux from the heater surface. Table 5 provides correspondence among

Table 5
Correspondence between power input and surface heat flux of the experimental heater and equivalent current through a copper conductor wire at 80°C having a diameter equal to that of the experimental heater ($D_{wire} = 6.35$ mm).

Heater power, q_H [W]	Surface heat flux from experimental heater, q''_s [W/m^2]	Equivalent current through charging wire, I_{wire} [A]
100	16446.04	692.32
200	32892.09	979.09
300	49338.13	1199.13
400	65784.17	1384.64
500	82230.22	1548.07
600	98676.26	1695.83
700	115122.31	1831.70
800	131568.35	1958.17
900	148014.39	2076.95
1000	164460.44	2189.30
1100	180906.48	2296.16
1200	197352.52	2398.26

total power input, surface heat flux of the experimental heater, and equivalent current through a copper conductor wire at 80°C having a diameter equal to that of the experimental heater ($D_{wire} = 6.35$ mm).

After each test reaches steady state conditions, at least 120 s of recorded temporal datapoints are averaged to yield a single steady state datapoint. Thermophysical properties of HFE-7100 are provided by the manufacturer, 3M Corporation. Fluid enthalpies at the inlet and outlet of the module are determined from the relations

$$h_{in} = h_f\big|_{T_{in}} + v_f\big|_{T_{in}}\left(P_{in} - P_{sat}|_{T_{in}}\right), \tag{6}$$

and

$$h_{out} = h_{in} + \frac{q''_s A_h}{\dot{m}}, \tag{7}$$

respectively, where h_f, v_f, and P_{sat} are based on the inlet fluid temperature, and Eq. (7) is obtained by applying an energy balance to the entire module. For all data collected from the present experiments, $h_{in} < h_f|_{P_{in}}$ and $h_{out} < h_f|_{P_{out}}$, indicating that the fluid is subcooled at both the module inlet and outlet and thereby the flow is subcooled throughout the module. Inlet and outlet thermodynamic equilibrium qualities are determined using the relation

$$x_e = \frac{h - h_f\big|_P}{h_{fg}\big|_P}, \tag{8}$$

where $h = h_{in}$ or h_{out} is the actual fluid enthalpy at the module inlet/outlet, and h_f and h_{fg} are based on the measured inlet/outlet plenum pressure. Subcooling at the inlet and outlet is calculated from

$$\Delta T_{sub} = T_{sat}|_P - T_f, \tag{9}$$

where $T_f = T_{in}$ or T_{out} is the corresponding measured fluid temperature, and T_{sat} is the saturation temperature corresponding to the inlet/outlet pressure.

The heated surface is divided into five unit-cells with a surface thermocouple situated at the center of each as shown in Fig. 5(a). Axial conduction through the heater is assumed negligible and the surface heat flux, q''_s, axially uniform. Local heat transfer coefficients are determined from the relation

$$h_z = \frac{q''_s}{T_{s,z} - T_{f,z}}, \tag{10}$$

where $T_{s,z}$ is the measured heater surface temperature and $T_{f,z}$ the local fluid temperature at the same axial location. $T_{f,z}$ is estimated from a linear interpolation between the inlet (measured T_{in}) and outlet (estimated from T_{in} by energy balance assuming only sensible heat transfer) fluid temperatures. The average heat transfer coefficient is then calculated based on an area-weighted average of the local heat transfer coefficients as

$$\bar{h} = \frac{\sum A_{s,z} h_z}{A_h} = \frac{\sum L_z h_z}{L_h}, \tag{11}$$

where $A_{s,z}$ and L_z are, respectively, the heated surface area and length of each unit cell, and A_h and L_h are, respectively, the total heated surface area and total heated length, as indicated in Fig. 5(a). Average surface temperature, $\bar{T}_s$, is also calculated in a similar manner.

Some of the key parameters of this study lie in the ranges given in Table 6. It is emphasized that although some parameters are expressed in various units throughout this paper for an easy understanding, all calculations are performed using SI units.

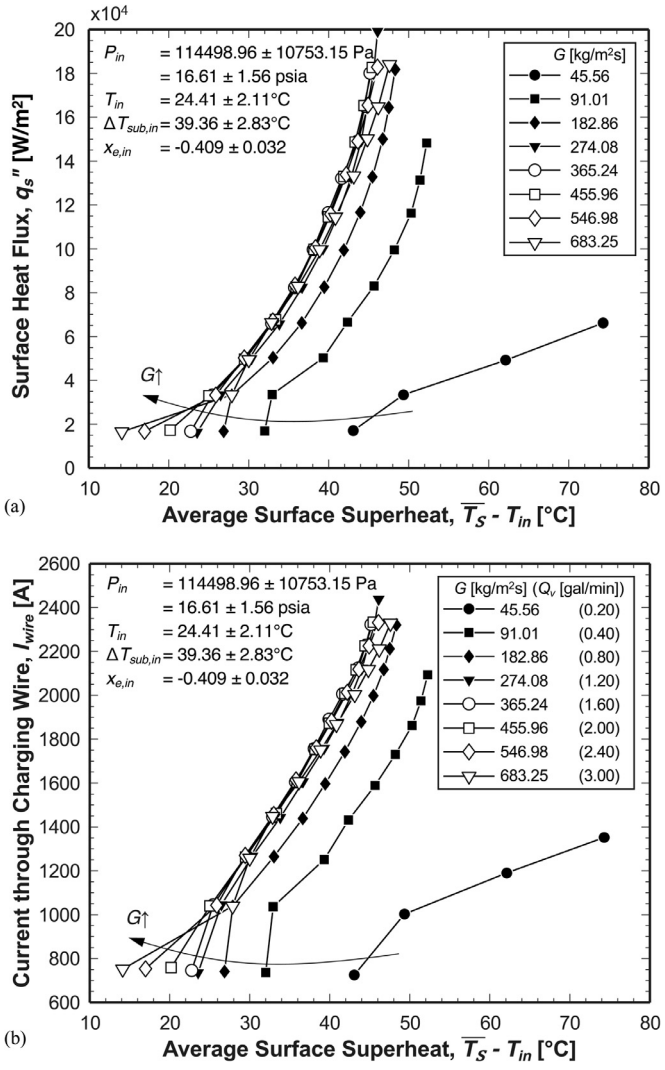

Fig. 6. Variations of (a) surface heat flux and (b) equivalent current through charging wire with average surface superheat for different mass velocities.

3. Experimental results and discussion

3.1. Overall heat transfer performance

Boiling curves, plotted as variations of surface heat flux with surface superheat, are a general means of displaying heat transfer performance of a two-phase thermal management system. Fig. 6(a) shows a set of averaged boiling curves for various mass velocities ranging from $G = 45.56$ to 683.25 kg/m^{2}s. It is noted that surface

Table 6
Summary of key parameters of present experiments.

Mass velocity, G	45.51 – 730.50 kg/m^{2}s
Volumetric flow rate, Q_v	1.250×10^{-5} – 2.020×10^{-4} m^3/s (0.20 – 3.20 gal/min)
Inlet pressure, P_{in}	102,999 – 142,392 Pa (14.94 – 20.65 psia)
Outlet pressure, P_{out}	102,061 – 140,218 Pa (14.80 – 20.34 psia)
Surface heat flux, q''_s	16,309 – 199,210 W/m^2
Inlet temperature, T_{in}	20.33 – 29.23°C
Inlet subcooling, $\Delta T_{sub,in}$	33.83 – 48.68°C
Inlet quality, $x_{e,in}$	-0.516 – -0.349
Outlet temperature, T_{out}	21.00 – 44.96°C
Outlet subcooling, $\Delta T_{sub,out}$	17.83 – 47.69°C
Outlet quality, $x_{e,out}$	-0.504 – -0.185
Average surface temperature, T_s	36.24 – 96.02°C
Equivalent current through charging wire, I_{wire}	725.61 – 2437.91 A

superheat is typically defined as $\Delta T_{sat} = T_s - T_{sat}$, but $T_s - T_{in}$ is used here due to the bulk fluid being subcooled throughout the module. Additionally, the average superheat in Fig. 6(a) is defined as $\bar{T}_s - T_{in}$, where $\bar{T}_s$ is the surface area average of all unit cell surface temperatures. For all mass velocities, the average surface superheat increases with increasing surface heat flux, with larger increases achieved at lower heat fluxes. The reduced rate of increase of surface temperature at higher heat fluxes is attributed to a reduction in single-phase liquid convection length and increasing portion of the heated surface incurring subcooled flow boiling, clearly a manifestation of increased contribution of latent heat transfer to total heat dissipation. At the highest heat fluxes of ~18 W/cm^2, the curves become almost vertical, indicating that surface temperature is maintained fairly constant for a range of heat fluxes; this is one of the fundamental benefits of all thermal management schemes utilizing boiling.

Considering the lowest heat flux of $q''_s \approx 2$ W/cm^2, it is clear that the surface superheat monotonically decreases with increasing mass velocity. This is due to the flow being single-phase throughout the module, as will be discussed in section 3.4. But for higher heat fluxes, this monotonicity vanishes with a clear decreasing trend apparent only for the lower mass velocities of $G = 45.56$, 91.01, 182.86, and 274.08 kg/m^{2}s. A drastic reduction in the average surface temperature is realized by doubling the mass velocity from 45.56 to 91.01 kg/m^{2}s. A further doubling of G to 182.86 kg/m^{2}s does induce a reduction but by a smaller amount. But for $G \geq 274.08$ kg/m^{2}s, the boiling curves seem to overlap one another. This is due to the dominance of latent heat over sensible heat transfer; the former being independent of mass velocity and the latter strongly dependent on flow velocity [41,53,55,72].

It is noted that, for the lowest two mass velocities of $G = 45.56$ and 91.01 kg/m^{2}s, further increases in heat flux were not experimentally feasible due to CHF occurrence. Flow rate essentially affects only the lower heat flux region and value of CHF [41]. Some researchers [43,51,53] have pointed to the presence of a hysteresis region in the lower heat flux, manifest by different boiling curves when increasing versus decreasing the heat flux. This phenomenon is beyond the scope of the present study.

The relationship between the surface heat flux, q''_s, and equivalent current through the charging wire, I_{wire}, is captured in Eqs. (3) – (5), which show heat flux roughly increases as the square of I_{wire}, although wire temperature has a rather significant impact on resistivity of the wire. The same datapoints in Fig. 6(a) are plotted in Fig. 6(b) as variations of I_{wire} with average surface superheat; these are henceforth termed 'pseudo' boiling curves. These curves are more relevant to the present application of EV charging wire cooling. The general trends are similar to those in Fig, 6(a), but the 'pseudo' boiling curves are more linear than the actual boiling curves, *i.e.*, average surface temperature increases almost linearly with I_{wire} for $I_{wire} > 1000$ A. The lowest I_{wire} of ~750 A results in single-phase convection all along the heated length, this is where G has the strongest influence on average surface temperature. For a fixed I_{wire}, Fig. 6(b) indicates that the heat transfer performance ceases to improve with increasing in G above 274.08 kg/m^{2}s. However, it should be kept in mind that G should be kept high enough to preclude CHF occurrence, especially in the downstream region of practical long heating wires.

3.2. Average heat transfer coefficient

Heat transfer coefficient, h, is an effective measure of the heat transfer performance of a thermal management system. The higher the heat transfer coefficient, the higher is the heat dissipation rate for a particular set of surface and bulk fluid temperatures. Fig. 7(a) shows the variation of average h over the entire heating surface with surface heat flux. For the lowest $q''_s \approx 2$ W/cm^2, average h increases monotonically with increasing G (or Re), a key characteristic of single-phase heat transfer. For higher heat fluxes, the curves for $G = 91.01$ – 683.25 kg/m^{2}s overlap with one another, meaning h becomes a weak function of G. This can be explained by ability of the fluid to absorb a major portion of the heat by nucleate boiling and dominance of latent heat transfer [41,51,53]. Fig. 7(a) also shows h increasing almost linearly for $q''_s > 2$ W/cm^2, a key characteristic of nucleate boiling heat transfer, as opposed to that for single-phase convection, where h is independent of heat flux. Notice that, for the highest mass velocity of $G = 683.25$ kg/m^{2}s and lowest two heat fluxes, the curve is horizontal, indicating the flow is maintaining purely single-phase convection.

Fig. 7(b) shows the same datapoints plotted as variations of average h with equivalent current, I_{wire}, and captures the same general trends manifest in Fig. 7(a). As I_{wire} is increased, the average heat transfer coefficient increases in a slightly concave upwards manner. Again, for all G values tested, the heat transfer coefficient increases with increasing G for the lowest $I_{wire} \approx 750$ A because of dominance of single-phase convection effects.

Since the test module is long enough to observe multiple flow regime transitions (single-phase liquid to PDB to FDB), the average heat transfer coefficient for most cases encompasses the net effects of multiple flow regimes, and sharp transition points are not apparent.

3.3. Local 'pseudo' boiling curves

Figs. 8(a) and 8(b) show local 'pseudo' boiling curves for two flow rates, $Q_v = 0.60$ and 2.80 gal/min, respectively. These are plotted as equivalent current through charging wire against the difference between local wire surface and inlet fluid temperatures. In Fig. 8(a), except for an erroneous datapoint corresponding to the lowest I_{wire}, the curves are linear for low I_{wire} and become concave upwards with increasing I_{wire}, especially for the downstream curves. A weaker concave upwards trend for the upstream location of $z = 0.0254$ m is indicative of dominance of single-phase

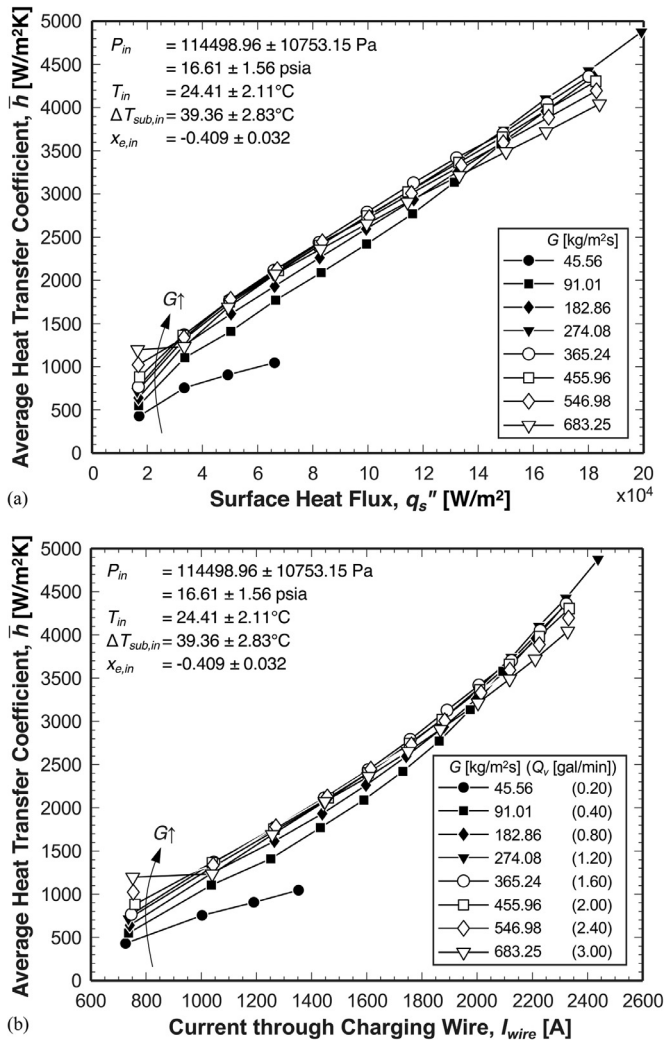

Fig. 7. Variations of average heat transfer coefficient with (a) surface heat flux and (b) equivalent current through charging wire for different mass velocities.

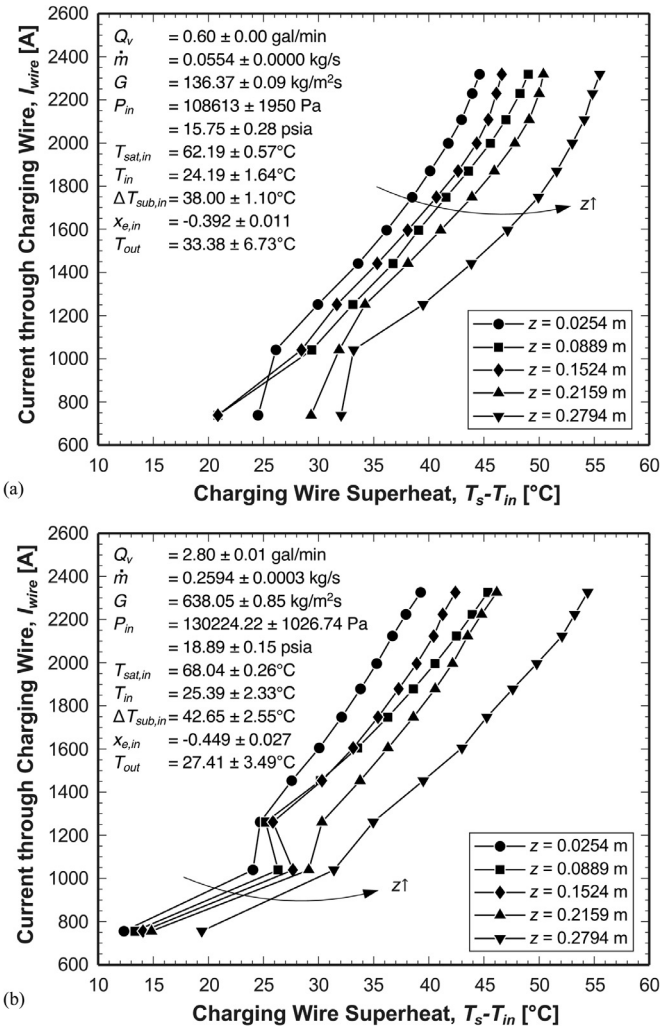

Fig. 8. Local 'pseudo' boiling curves for (a) $G = 136.37$ kg/m²s ($Q_v = 0.6$ gal/min) and (b) $G = 638.05$ kg/m²s ($Q_v = 2.8$ gal/min), for different axial locations.

convection effects. Considering the downstream most location of $z = 0.2794$ m, transition to FDB is predicted to occur at $I_{wire} \approx$ 1870 A. There is very little change in surface superheat in the FDB regime over a wide range of heat fluxes [72].

The curves in Fig. 8(b) follow the same trends as those in Fig. 8(a) but are more linear for higher I_{wire} values. All 5 curves show a slight kink around $I_{wire} \approx 1000$ A, likely the outcome of a small surface temperature overshoot at ONB [43]. But as soon as bubbles nucleate following ONB, the latent heat transfer brings the surface temperature down.

3.4. Demarcation between flow regimes

Demarcation between flow regimes within the test module is needed for a better understanding of the underlying heat transfer physics and for guiding final design of the EV charging cable cooling system. Operating conditions are chosen such that the coolant enters the module in a subcooled liquid state and remains subcooled throughout the module. A detailed description of the different flow regimes encountered in subcooled flow boiling has already been provided in Section 1.4. As the subcooled liquid flows over the heated section of the heater, it gains sensible heat and the bulk fluid and surface temperatures increase. The first bubbles are formed at the axial location where the local surface temperature exceeds the temperature corresponding to ONB, $T_s > T_{s,ONB}$. The boiling inception occurs at cavities having a radius equal to that corresponding to tangency between the superheat 'required' to grow bubbles beyond the mouth of a cavity and the superheat 'available' in the liquid boundary layer adjacent to the heated surface [57]. $T_{s,ONB}$ is determined by equating the 'required' superheat to the 'available' superheat at a cavity. Cavities having radii both smaller and larger than the tangency radius are gradually activated downstream of ONB because of increased availability of wall superheat. In the single-phase liquid convection region, the heat transfer coefficient is determined from

$$q_s'' = h(T_s - T_f), \tag{12}$$

and the heat flux required to initiate ONB is given by Sato and Matsumura's relation [59],

$$q_{ONB}'' = \frac{k_f h_{fg}(T_s - T_{sat})^2}{8\sigma T_{sat} v_{fg}}, \tag{13}$$

Equation (13) can be combined with Eq. (12) to yield a relation capturing the effect of convection on $T_{s,ONB}$,

$$T_{s,ONB} = T_{sat} + \frac{4\sigma T_{sat} v_{fg} h}{k_f h_{fg}}\left(1 + \sqrt{1 + \frac{k_f h_{fg}}{2\sigma T_{sat} v_{fg} h}(T_{sat} - T_f)}\right). \tag{14}$$

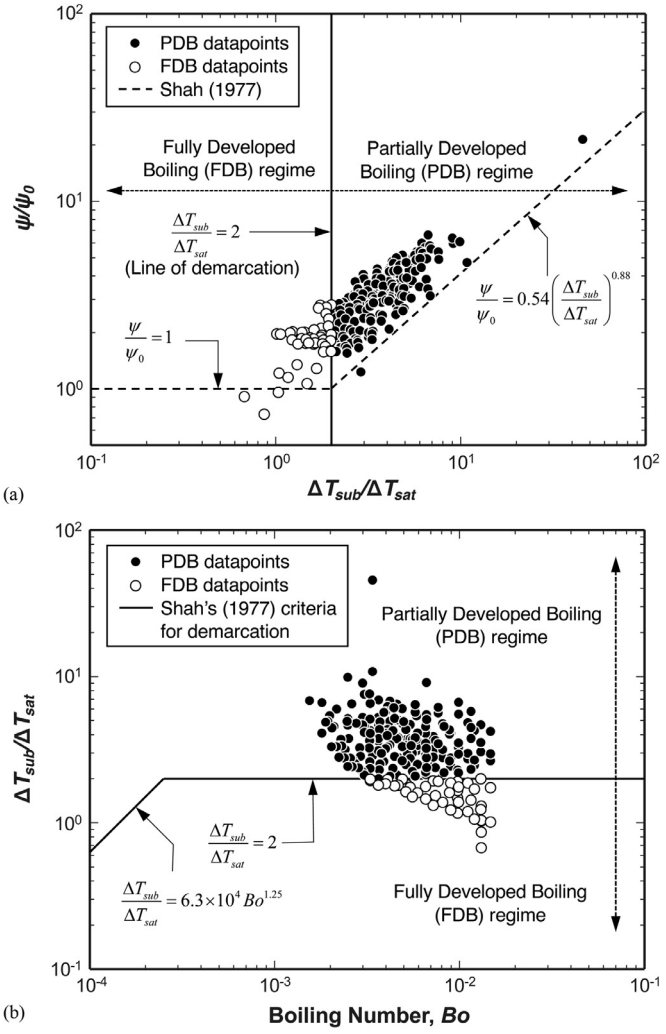

Fig. 9. Demarcation of experimental subcooled boiling datapoints into Partially Developed Boiling and Fully Developed Boiling based on Shah's [62] relations: (a) ψ/ψ_0 versus $\Delta T_{sub}/\Delta T_{sat}$, and (b) $\Delta T_{sub}/\Delta T_{sat}$ versus boiling number, *Bo*.

Shah's [62] criterion for transition from PDB to FDB is widely accepted in the literature and is given by

$$\text{PDB(high subcooling)}: \frac{\Delta T_{sub}}{\Delta T_{sat}} = \frac{T_{sat}-T_f}{T_s-T_{sat}} > 2 \text{ or } \frac{\Delta T_{sub}}{\Delta T_{sat}} > 6.3\times10^4 Bo^{1.25} \quad (15)$$

and

$$\text{FDB(low subcooling)}: \frac{\Delta T_{sub}}{\Delta T_{sat}} \le 2 \text{ and } \frac{\Delta T_{sub}}{\Delta T_{sat}} \le 6.3\times10^4 Bo^{1.25}, \quad (16)$$

where *Bo* is the Boiling number, defined as

$$Bo = \frac{q''_s}{Gh_{fg}}. \quad (17)$$

Fig. 9 shows the process of demarcating all experimental subcooled boiling datapoints into PDB and FDB according to the Shah criterion. Fig. 9(a) shows a plot of ψ/ψ_0 versus $\Delta T_{sub}/\Delta T_{sat}$, ratio of local subcooling to surface superheat, where ψ is a measure of the contribution of latent to total heat transfer and is defined as the ratio of actual surface heat flux to an estimated heat flux based on single-phase heat transfer coefficient and wall superheat. In the same figure, ψ_0 is the value of ψ at $x_e = 0$ (zero subcooling and zero equilibrium quality), which is a function of boiling number,

$$\psi_0 = \begin{cases} 230Bo^{0.5}, & Bo > 0.3\times10^{-4} \\ 1+46Bo^{0.5}, & Bo < 0.3\times10^{-4} \end{cases}. \quad (18)$$

Except for a few stray datapoints, the plot indicates that the datapoints change their general trend about a transition value of $\Delta T_{sub}/\Delta T_{sat} = 2$, with most datapoints below 2 acquiring near zero slope and those above 2 a positive slope. This trend is similar to one predicted according to a transition relation by Shah based on a very comprehensive database [62], which is given by

$$\frac{q''_s/(h_{sp}\Delta T_{sat})}{\psi_0} = \frac{\psi}{\psi_0} = \begin{cases} 0.54\left(\frac{\Delta T_{sub}}{\Delta T_{sat}}\right)^{0.88}, & \frac{\Delta T_{sub}}{\Delta T_{sat}} > 2 \\ 1, & \frac{\Delta T_{sub}}{\Delta T_{sat}} \le 2 \end{cases}, \quad (19)$$

where h_{sp} is single-phase heat transfer coefficient given by the Dittus-Boelter equation,

$$\frac{h_{sp}D}{k_f} = Nu_{sp} = 0.023\mathrm{Re}_f^{0.8}\mathrm{Pr}_f^{0.4}. \quad (20)$$

The constant offset of the present experimental data from Shah's reference lines in Fig. 9(a) can be explained by impact of differences between present annular flow configuration and flow in a circular tube on the turbulent single-phase heat transfer coefficient. By plotting $\Delta T_{sub}/\Delta T_{sat}$ against *Bo*, Fig. 9(b), the transition between PDB and FDB becomes clearer. PDB datapoints are clustered above the $\Delta T_{sub}/\Delta T_{sat} = 2$ line and FDB datapoints below. This is the same as Shah's transition criteria given by Eqs. (15) and (16). However, the present datapoints are associated with high Boiling numbers, therefore Shah's second transition line, $\Delta T_{sub}/\Delta T_{sat} = 6.3\times10^4 Bo^{1.25}$, does not play a role in the demarcation of any datapoint.

Another popular method of determining the transition from PDB to FDB is based on the net vapor generation point, where bubbles begin to depart from the heated surface [64]. Saha and Zuber [63] used this premise to develop the following criterion for transition to FDB,

$$\text{PDB (high subcooling)}: \Delta T_{sub} > \begin{cases} 0.0022\left(\frac{q''_s D_e}{k_f}\right), & Pe < 70000 \\ \frac{153.8q''_s}{Gc_{p,f}}, & Pe > 70000 \end{cases}, \quad (21)$$

where *Pe* is Peclet number ($RePr_f$). This criterion was tested against the present experimental data and resulted in unphysical flow regime transitions along the flow direction. This can be explained as follows. *Pe* is fairly constant along the flow direction since property changes are too small to influence the results. For a particular flow rate, Saha and Zuber's ΔT_{sub} corresponding to PDB is directly proportional to the surface heat flux and fairly constant along the flow direction. For many cases, the predicted transition point fell well within the single-phase flow region and the flow was found to transition directly from single-phase liquid to FDB, bypassing the PDB region altogether. These facts render their PDB-FDB transition criterion unsuitable for the present application despite recommendation to the contrary by other researchers [64,65].

Therefore, it was decided that demarcation of flow regimes in the present study be based on a combination of ONB criterion from Eq. (14) and Shah's criteria for transition from PDB and FDB. The results are presented in Fig. 10 in the form of flow regime contour maps. In all, there are 820 experimental datapoints which are demarcated into 585 single-phase, 190 PDB, and 45 FDB datapoints. Fig. 10(a) shows a map of the flow regimes for a constant mass velocity of $G = 136.37$ kg/m^{2}s (flow rate of $Q_v = 0.60$ gal/min). The vertical axis represents heat flux from the inner heating surface and the horizontal axis axial position along the flow direction. For lower heat fluxes, the flow is single-phase throughout the module with no bubble nucleation. As the heat flux is increased, the

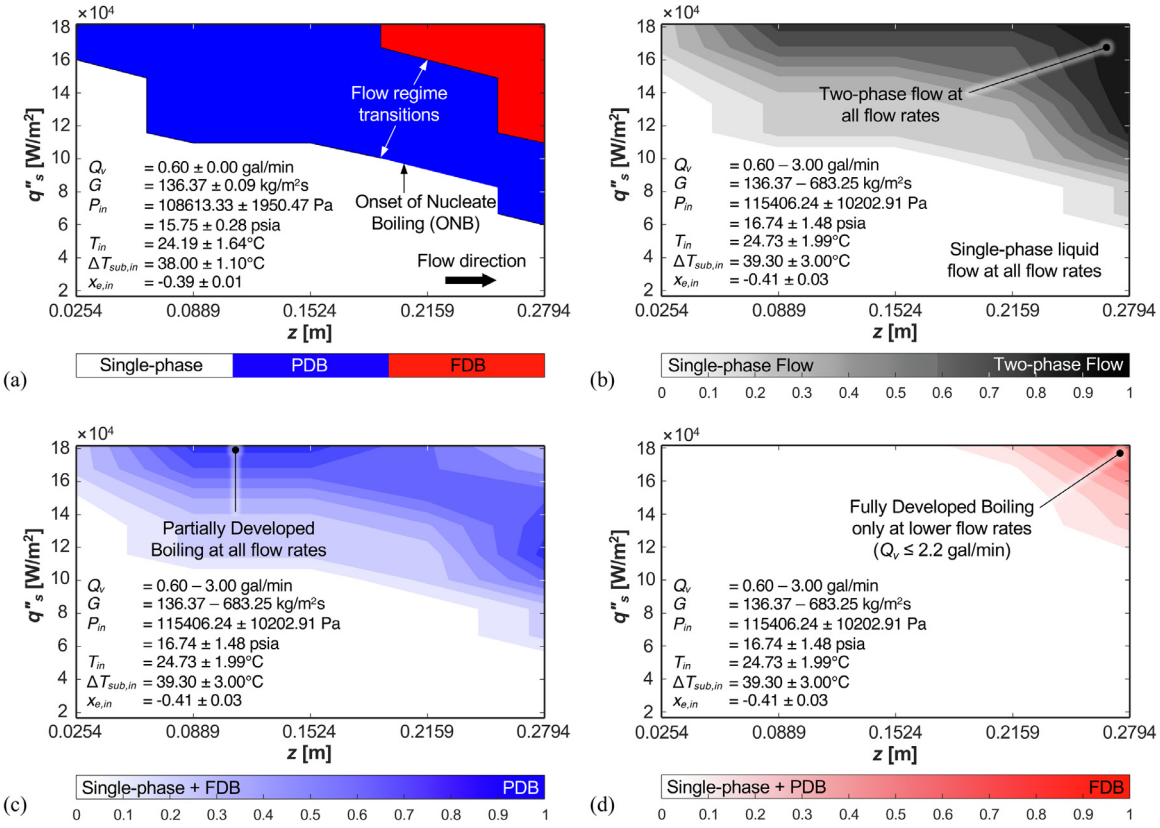

Fig. 10. Flow regime contour maps indicating (a) demarcation of flow regimes for a fixed mass velocity of $G = 136.37$ kg/m^{2}s ($Q_v = 0.60$ gal/min), and, for a mass velocity range of $G = 136.37$ – 683.25 kg/m^{2}s, (b) transition from single-phase flow to two-phase flow based on ONB, (c) PDB dominant regions, and (d) FDB dominant regions. Darker colors in (b), (c), and (d) indicate the corresponding flow regime is dominant over a wider mass velocity range.

location of ONB moves upstream and the flow downstream transitions from single-phase liquid convection to PDB. With a further increase in the heat flux, transition from PDB to FDB is seen downstream and, once again, location of this transition moves upstream with increasing heat flux. Fig. 10(b) shows the point of ONB predicted according to Eq. (14) for different mass velocities ranging from $G = 136.37$ to 683.25 kg/m^{2}s ($Q_v = 0.60$ – 3.00 gal/min). The regions that are fully blank (white) and fully black represent, respectively, single-phase and two-phase flow regimes at all flow rates. The intermediate gray tones indicate that the region is two-phase at lower flow rates and single-phase at higher flow rates, the darker the region, the greater number of flow rates resulting in two-phase flow regimes. It is clear that the point of ONB moves upstream as the high flux is increased. Figs. 10(c) and 10(d) show the demarcation of the two-phase datapoints into PDB and FDB, respectively, for the same operating conditions and mass velocity range as Fig. 10(b). Similar to Fig. 10(b), the darker the region the greater is the number of datapoints for that particular regime. Fig. 10(d) indicates that FDB occurs primarily in the downstream locations for higher heat fluxes and mostly low values of Q_v. For most of the lower heat fluxes, fully developed boiling is not seen for any flow rate. And, for the higher flow rate cases, FDB is not seen for the range of applied heat fluxes. These are the reasons for the plot not showing any region in solid red color.

3.5. Assessment of existing subcooled flow boiling correlations

Only a few correlations are available in the literature for subcooled flow boiling in an annulus. Based on an exhaustive literature survey, the authors found no correlations or experimental data for subcooled flow boiling of dielectric fluid HFE-7100 in a horizontal annulus. Therefore, an attempt is made to assess the applicability of previous subcooled flow boiling correlations to the flow configuration in this study. Table 7 summarizes the correlations investigated. Notice that some terms are rearranged for consistency among the different correlations. Correlations by Papell [73], Badiuzzaman [74], Moles and Shaw [75], and Shaw [51] were constructed in non-dimensional form as Nu_{sc}/Nu_{sp}, ratio of subcooled boiling to single-phase Nusselt numbers, which is also equal to the ratio of subcooled boiling to single-phase heat transfer coefficients, h_{sc}/h_{sp}. The correlations by Shah [62,64,68], Gungor and Winterton [69], and Liu and Winterton [71] offer the advantage of direct determination of the subcooled boiling heat transfer coefficient. The choice of auxiliary correlations for determining the single-phase and nucleate pool boiling heat transfer coefficients is based entirely on recommendations from the original studies.

In the assessment study, the thermophysical properties of HFE-7100 are evaluated at specific temperatures in the different subcooled boiling correlations based on how they were originally developed. For example, properties in the Dittus-Boelter equation are based on bulk liquid temperature [76,77], and properties in the Sieder-Tate equation are also based on bulk liquid temperature except for the liquid viscosity denominator, which is based on heated surface temperature [78]. The performance of each correlation in predicting the present experimental data is assessed using three different statistical parameters: Mean Absolute Error (MAE), and inliers θ and ξ. MAE is defined as

$$MAE\ (\%) = \frac{1}{N}\sum\left[\frac{|h_{pred} - h_{\exp}|}{h_{\exp}} \times 100\right], \tag{22}$$

and θ and ξ are, respectively, the percentages of datapoints predicted within ±30% and ±50% of the experimental values. Fig. 11 shows results of this assessment. Datapoints in all plots are segre-

Table 7
Subcooled flow boiling correlations.

Author(s)	Correlation	MAE	Remarks
Papell (1963) [73]	$\frac{Nu_{sc}}{Nu_{sp}} = 90\left(\frac{q''_s}{h_{fg}\rho_g U}\right)^{0.7}\left(\frac{h_{fg}}{c_{p,f}\Delta T_{sub}}\right)^{0.84}\left(\frac{\rho_g}{\rho_f}\right)^{0.756}$ $= 90\,Bo^{0.7}Ja^{**-0.84}(\rho_g/\rho_f)^{0.056}$ $Nu_{sp} = 0.021\,\mathrm{Re}_f^{0.8}\,\mathrm{Pr}_f^{0.4}$	63.49%	• Subcooled boiling in a uniformly heated Inconel X tube • Distilled water and ammonia • Single-phase heat transfer coefficient based on Colburn-type equation [83] with properties evaluated at film temperature • Specific heat capacity evaluated at mean of saturation and bulk fluid temperatures, and all other properties at saturation temperature
Badiuzzaman (1967) [74]	$\frac{Nu_{sc}}{Nu_{sp}} = C\left\{\left(\frac{q''_s}{h_{fg}\rho_g U}\right)\left(\frac{h_{fg}}{c_{p,f}\Delta T_{sub}}\right)^{1.2}\left(\frac{\rho_g}{\rho_f}\right)^{1.08}\left(\frac{\Delta T_{sub}}{T_{sat}}\right)^{0.6}\right\}^m$ $= C\{BoJa^{**-1.2}(\rho_g/\rho_f)^{0.08}(\Delta T_{sub}/T_{sat})^{0.6}\}^m$ Water: $C = 178$, $m = 0.75$ Organic fluids: $C = 759$, $m = 0.89$ (used in this study) $Nu_{sp} = 0.021\,\mathrm{Re}_f^{0.8}\,\mathrm{Pr}_f^{0.4}$	14.73%	• Subcooled boiling over a horizontal stainless steel 321 rectangular strip • Water, ethanol, and isopropanol • Specific heat capacity evaluated at mean of saturation and bulk fluid temperatures, and all other properties at saturation temperature • Single-phase heat transfer coefficient based on Colburn-type equation [83] with properties evaluated at film temperature
Moles & Shaw (1972) [75]	$\frac{Nu_{sc}}{Nu_{sp}} = 78.5\left(\frac{q''_s}{h_{fg}\rho_g U}\right)^{0.67}\left(\frac{h_{fg}}{c_{p,f}\Delta T_{sub}}\right)^{0.5}\left(\frac{\rho_g}{\rho_f}\right)^{0.7}\left(\frac{c_{p,f}\mu_f}{k_f}\right)^{0.46}$ $= 78.5Bo^{0.67}Ja^{**-0.5}(\rho_g/\rho_f)^{0.03}\,\mathrm{Pr}_f^{0.46}$ $Nu_{sp} = 0.027\mathrm{Re}_f^{0.8}\,\mathrm{Pr}_f^{1/3}\left(\frac{\mu_f}{\mu_f\vert_{T_s}}\right)^{0.14}\left(1+\left(\frac{D_e}{L_h}\right)^{0.7}\right)$ for $\frac{L_h}{D_e} < 60$	11.68%	• Subcooled boiling in vertical upflow in a circular tube, vertical upflow in rectangular channel, and horizontal flow over a heated strip • Single-phase heat transfer coefficient calculated using Seider-Tate equation modified for entrance effects [78] • Stainless steel 347, 304, 321, Inconel X, and nickel L and A • Water, ethanol, isopropanol, n-butanol, ammonia, aniline, and hydrazine • Prandtl number evaluated at mean film temperature, and all other properties at saturation temperature
Shaw (1972) [51]	$\frac{Nu_{sc}}{Nu_{sp}} = 82\left(\frac{q''_s}{h_{fg}\rho_g U}\right)^{0.68}\left(\frac{h_{fg}}{c_{p,f}\Delta T_{sub}}\right)^{0.5}\left(\frac{\rho_g}{\rho_f}\right)^{0.69}\left(\frac{c_{p,f}\mu_f}{k_f}\right)^{0.46}$ $= 82Bo^{0.68}Ja^{**-0.5}(\rho_g/\rho_f)^{0.01}\,\mathrm{Pr}_f^{0.46}$ $Nu_{sp} = 0.027\mathrm{Re}_f^{0.8}\,\mathrm{Pr}_f^{1/3}\left(\frac{\mu_f}{\mu_f\vert_{T_s}}\right)^{0.14}(1+\left(\frac{D_e}{L_h}\right)^{0.7})$ for $\frac{L_h}{D_e} < 60$	15.00%	• Subcooled boiling in vertical upflow in a circular tube, vertical upflow in rectangular channel, horizontal flow over a heated strip, and vertically upflow through a channel made of a circular tube placed along the center of a square tube • Single-phase heat transfer coefficient calculated using Seider-Tate equation modified for entrance effects [78] • Stainless steel 304, 321, and 347, Inconel X, and nickel L and A • Water, ethanol, isopropanol, n-butanol, ammonia, aniline, and hydrazine • Prandtl number evaluated at mean film temperature, and all other properties at saturation temperature
Shah (1983) [62,68]	$q''_s = h_{sc}(T_s - T_f) = \begin{cases}\left(\psi_0 + \frac{\Delta T_{sub}}{\Delta T_{sat}}\right)h_{sp}\Delta T_{sat}, & PDB\\ \psi_0 h_{sp}\Delta T_{sat}, & FDB\end{cases}$ $\psi_0 = \begin{cases}230Bo^{0.5}, & Bo > 0.3\times10^{-4}\\ 1+46Bo^{0.5}, & Bo < 0.3\times10^{-4}\end{cases}$ $\frac{h_{sp}D_e}{k_f} = Nu_{sp} = 0.023\mathrm{Re}_f^{0.8}\,\mathrm{Pr}_f^{0.4}$	55.03%	• Subcooled boiling in horizontal and vertical tubes, and vertical annuli • Single-phase heat transfer coefficient based on Dittus-Boelter equation [76,77] • Water, R-113, methanol in annuli; water, R-11, R-12, R-113, methanol, isopropanol, n-butanol, ammonia, and aqueous solution of potassium carbonate for other flow geometries • Copper, stainless steel, nickel, Inconel, and glass • Latent heat calculated at saturation temperature, and all other properties at bulk fluid temperature
Gungor & Winterton (1986) [69]	$q''_s = h_{sp}(T_s - T_f) + Sh_{nb}(T_s - T_{sat}) = h_{sc}(T_s - T_f)$ $\Rightarrow h_{sc} = h_{sp} + Sh_{nb}\frac{\Delta T_{sat}}{(T_s - T_f)}$ $\frac{h_{sp}D}{k_f} = Nu_{sp} = 0.023\mathrm{Re}_f^{0.8}\,\mathrm{Pr}_f^{0.4}$ $h_{nb} = 55P_R^{0.12}(-\log_{10}P_R)^{-0.55}M_W^{-0.5}q''^{0.67}_s$ $E = 1$; $S = (1 + 1.15\times10^{-6}E^2\mathrm{Re}_f^{1.17})^{-1}$ For horizontal tubes and :$Fr_f \le 0.05$ $E = EFr_f^{0.1-2Fr_f}$ and $S = SFr_f^{0.5}$ $Fr_f = \frac{G^2}{\rho_f^2 g D_h} = \frac{U^2}{gD_h}$	55.37%	• Subcooled boiling in vertical and horizontal tubes and annuli • Single-phase heat transfer coefficient based on Dittus-Boelter equation [76,77] • Nucleate boiling heat transfer coefficient based on Cooper equation [84] • Water, refrigerants, and ethylene glycol

(*continued on next page*)

Table 7 (*continued*)

Author(s)	Correlation	MAE	Remarks
Liu & Winterton (1991) [71]	$q''_s = ((Eh_{sp}(T_s - T_f))^2 + (Sh_{nb}\Delta T_{sat})^2)^{0.5} = h_{sc}(T_s - T_f)$ $\Rightarrow h_{sc} = \left((Eh_{sp})^2 + \left(\frac{Sh_{nb}\Delta T_{sat}}{T_s - T_f}\right)^2\right)^{0.5}$ $\frac{h_{sp}D}{k_f} = Nu_{sp} = 0.023\mathrm{Re}_f^{0.8}\mathrm{Pr}_f^{0.4}$ $E = 1\ S = (1 + 0.055E^{0.1}\mathrm{Re}_f^{0.16})^{-1}$ $h_{nb} = 55P_R^{0.12}(-\log_{10}(P_R))^{-0.55}M_W^{-0.5}q''^{0.67}$ For horizontal tubes and :$Fr_f \le 0.05\ E = EFr_f^{0.1-2Fr_f}$ and $S = SFr_f^{0.5}$	68.01% using D_h; 70.64% using D_{hp}	• Subcooled boiling in vertical and horizontal tubes and annuli • Single-phase heat transfer coefficient based on Dittus-Boelter equation [76,77] • Nucleate boiling heat transfer coefficient based on Cooper equation [84] • Water, refrigerants, ethylene glycol, ethanol and n-butanol • Liquid Reynolds and Prandtl numbers are calculated at bulk fluid temperature, and all other properties at saturation temperature
Shah (2017) [64]	$q''_s = h_{sc}(T_s - T_f) = \begin{cases} \frac{\psi_0 h_{sp}(\Delta T_{sat} - 1.65\Delta T_{sub}^{-0.44})}{0.67}, & PDB \\ \psi_0 h_{sp}\Delta T_{sat}, & FDB \end{cases}$ $\psi_0 = \begin{cases} 230Bo^{0.5}, & Bo > 0.3\times10^{-4} \\ 1 + 46Bo^{0.5}, & Bo < 0.3\times10^{-4} \end{cases}$ $\frac{h_{sp}D}{k_f} = Nu_{sp} = 0.023\mathrm{Re}_f^{0.8}\mathrm{Pr}_f^{0.4}$	50.16%	• Subcooled boiling in channels of various geometries and annuli of different heating configurations; horizontal and vertical flows • Single-phase heat transfer coefficient based on Dittus-Boelter equation [76,77] • 13 different fluids (water, refrigerants, chemicals) • Stainless steel, copper, brass, zirconium-copper alloy, nickel, Inconel, and glass • Latent heat calculated at saturation temperature, and all other properties at bulk fluid temperature

gated into PDB and FDB using solid and open markers, respectively. The major outliers in all these plots are in the lower-left corner and mostly belong to lower flow rate cases. This may be explained by inability of very low flow rates in a horizontal annulus or channel to ensure symmetry in vapor formation and distribution, as buoyancy stratifies the vapor upwards to the top of the annulus. This stratification effect is absent at high flow rates, where high inertia of the incoming liquid dwarfs any buoyancy effects.

Fig. 11(a) shows the Papell's correlation yields poor accuracy, with relatively high MAEs of 65.00% and 57.11% in the PDB and FDB regimes, respectively. Datapoints follow a linear trend below the reference lines, indicating that all datapoints are offset by almost the same percentage. This can be attributed to its development based on data for water and liquid ammonia whose thermophysical properties are very different from those of HFE-7100. The original correlation also did not consider flow in annuli. Badiuzzaman's correlation, Fig. 11(b), is a modified form of Papell's correlation, using an additional term and different empirical constants. As shown in Fig. 11(b), predictions of the Badiuzzaman' correlation are very close to the experimental data with only a few FDB outliers reducing overall accuracy. Better predictions are the result of reliance on data for alcohols that possess properties similar to those of HFE-7100. As shown in Fig. 11(c), Moles and Shaw's correlation gives the best predictions of the present data, with an overall MAE of only 11.68%. The success of this correlation is attributed to its development being based on a wide variety of flow configurations and fluids. It employs dimensionless groups similar to Papell's but with different empirical constants and additional of a liquid Prandtl group. The single-phase Nusselt number used to assess Moles and Shaw's correlation is calculated using the Seider-Tate equation modified for an entrance effect because the length of our annulus is short compared to its effective diameter.

Interestingly, Moles and Shaw's correlation gave the best predictions for R-134a flow through microchannels in a recent study by the present authors [39]. As seen in Fig. 11(d), Shaw's correlation, which is based on the same formulation and database as Moles and Shaw's but with additional data for upflow in square-round annulus, yields slightly higher predictions but with a somewhat similar trend. Figs. 11(e) and 11(f) show both correlations by Gungor and Winterton and by Liu and Winterton exhibit large deviations from the data, with overall MAEs of 55.37% and 68.01%, respectively. Both correlations were originally developed for saturated flow boiling following an earlier formulation by Chen [79], but with different enhancement and suppression factors. They were then modified for subcooled flow boiling by setting the enhancement factor equal to unity (in the absence of net vapor generation) and achieved decent predictions against subcooled boiling data for both tubes and annuli. In both correlations, the single-phase and nucleate pool boiling heat transfer coefficients are calculated using Dittus-Boelter and Cooper's equations, respectively. It should also be mentioned that Liu and Winterton's correlation involves a root-sum-square combination of single-phase and nucleate boiling terms rather than just the sum of the two. And, although Liu and Winterton [71] suggested use of heated perimeter diameter over hydraulic diameter to obtain better predictions from their correlation, the MAE worsened, from 68.01% to 70.64%. Figs. 11(g) and 11(h) show Shah's old (1983) [68] and new (2017) [64] correlations for subcooled boiling also show large deviations, with MAEs of 55.03% and 50.16%, respectively. These correlations are different from the other correlations in that they require initial demarcation of subcooled boiling regimes and include two different equations for predicting PDB and FDB data. The large MAEs of these correlations is surprising considering that both were developed for a wide range of subcooled flow boiling configurations and diverse fluids (the later correlation being based on a bigger database). Also surprising is that the two correlations are based on databases that include flow in annuli. One possible reason for the rather poor predictions is that the databases Shah used to develop his correlations include annuli with annular gaps much smaller than those of the present, excepting data by Hasan *et al.* [53] which Shah included in his later database.

Other recent correlations for subcooled flow boiling in conventional channels include those by Prodanovic *et al.* [80] based on Moles and Shaw's, Baburajan *et al.* [81] based on three dimensionless groups from Moles and Shaw's, and Yan *et al.* [82] and Zhu *et al.* [72] based on Chen's. But these correlations were developed for very narrow ranges of operating conditions using water alone and were therefore not considered for assessment.

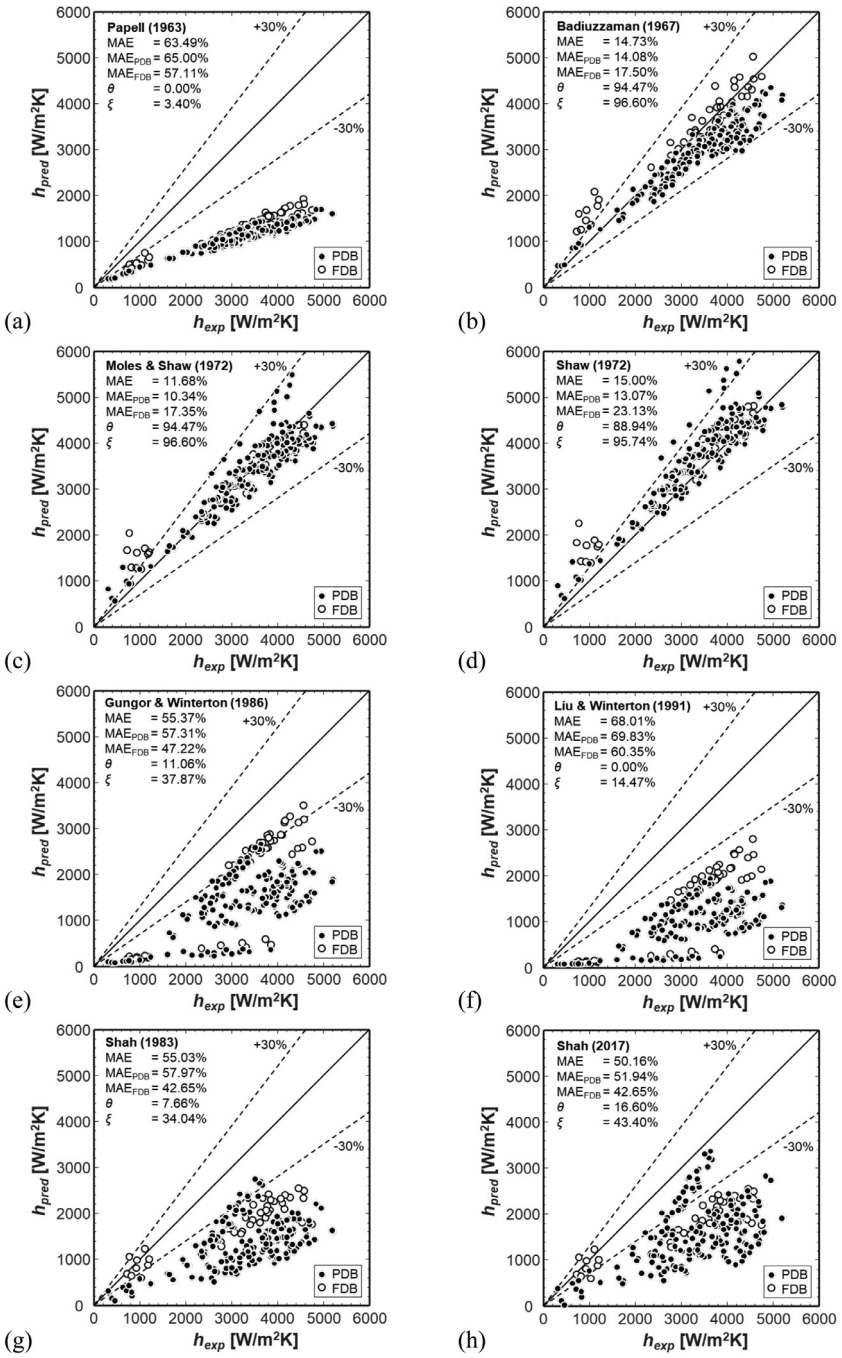

Fig. 11. Comparison of experimental data for flow in an annulus to predictions of subcooled boiling correlations of (a) Papell [73], (b) Badiuzzaman [74], (c) Moles and Shaw [75], (d) Shaw [51], (e) Gungor and Winterton [69], (f) Liu and Winterton [71], (g) Shah (1983) [68], and (h) Shah (2017) [64].

3.6. Miscellaneous remarks on thermal management system

In this section, some miscellaneous remarks on the final thermal management system are given. Figs. 12(a) and 12(b) show representative temporal records of temperatures within the test module for a flow rate of $Q_v = 3.00$ gal/min and heat fluxes of 16,520.23 and 183,980.86 W/m^2, respectively. The corresponding electrical current values are 751.64 and 2328.25 A, and these denote the lowest and highest values tested for this flow rate. For both cases, there is a uniform heat flux increase of ~16,520 W/m^2 at $t = 0$ s. As expected, for the lower heat flux case, this is similar to a 'cold start' and there is a larger initial temperature jump and the system reaches steady state within a few seconds of transience. For this lower heat flux case, the flow is fully single-phase throughout the module, with all the wire surface temperatures, T_s, being lower than the saturation temperature, T_{sat}, corresponding to the pressure within the module. The outlet fluid temperature is slightly higher than the inlet, and the surface temperature increases in the flow direction. Minuscule aberrations in the temperature readings are due to noise from the main AC lines. In Fig. 12(b), the jump in temperatures at $t = 0$ s is smaller and again the system reaches steady state within a few seconds. This case has boiling occurring over a portion of the wire, with $T_s > T_{sat}$. The outlet fluid temperature is higher than the inlet because of the heat supplied to the fluid. For both cases, T_s increases along the flow direction and the charging wire is at a safe temperature below ~85°C. Moreover, the

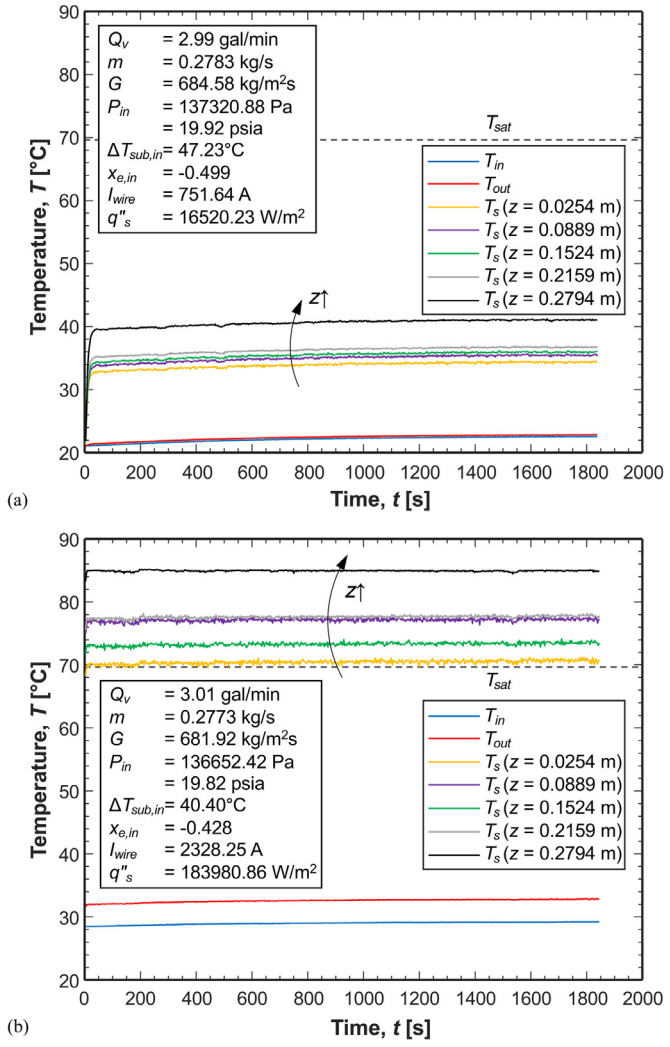

Fig. 12. Temporal records of temperatures within the module for $Q_v = 3.00$ gal/min and charging wire currents of (a) $I_{wire} = 751.64$ A and (b) $I_{wire} = 2328.25$ A.

external insulating conduit would be at a temperature well below the outlet fluid temperature, allowing safe human handling of the charging cable in its entirety. The fast adaptability of the system to variations in charging wire current is mainly due to the lower thermal mass of the wire. Finally, two-phase instabilities such as pressure drop oscillations *etc*. did not manifest during any of the present experiments.

4. Conclusions

This study explored a thermal management scheme for ultra-fast electric vehicle charging cables which relies on subcooled flow boiling. Experiments were performed by mimicking the heat generated within a 6.35-mm diameter wire for continuous current values ranging from 726 A to 2438 A. Highly subcooled dielectric liquid HFE-7100 was pumped through a 304.8-mm long horizontal concentric circular annulus consisting of a uniformly heated inner surface and adiabatic outer tube of respective diameters 6.35 mm and 23.62 mm. Key findings are summarized as follows:

(1) Averaged boiling curves indicate surface heat flux to increase with average surface superheat, but with the increase becoming smaller at large heat fluxes. Charging wire current increases almost linearly with wire superheat. For lower heat fluxes, superheat decreases monotonically with increasing mass velocity, indicating prevalence of single-phase regime. For higher heat fluxes, superheat decreases with increasing mass velocity until a certain threshold, after which mass velocity has a rather insignificant impact on surface superheat.

(2) Except for the fully single-phase regime, the average heat transfer coefficient increases almost linearly with increasing surface heat flux, and in a slightly concave upwards manner with increasing charging wire current; mass velocity has a rather insignificant effect. In the fully single-phase regime, heat transfer coefficient is independent of heat flux or charging current and monotonically increases with increasing mass velocity alone.

(3) For all operating conditions, the local surface superheat generally increases along the flow direction.

(4) The 820 datapoints from the present experimental study were demarcated into single-phase liquid convection, partially developed boiling, and fully developed boiling regimes, and flow regime contour maps specific to the study were developed. Generally, the points of transition between regimes advance upstream with increasing heat flux but downstream with increasing mass velocity.

(5) The predictive performances of several prior subcooled flow boiling heat transfer correlations were tested against the experimental PDB and FDB data. Moles and Shaw's [75] correlation, used with the hydraulic diameter of the annulus, yielded the best predictions, evidenced by an overall MAE of only 11.68%.

(6) Temporal records indicate the adaptability and stability of the thermal management system for both single-phase liquid convection and subcooled boiling.

(7) Overall, it is shown experimentally that subcooling flow boiling could be utilized to cool down ultra-fast EV charging cables carrying up to 2438 A continuous current, which is roughly four times higher than with the present-day fastest commercial charger.

Declaration of Competing Interest

None. The authors declare that they have no known competing financial interests or personal relationships that could have appeared to influence the work reported in this paper.

Acknowledgement

The authors acknowledge the support of the Ford – Purdue University Alliance under grant no. 40002059.

References

[1] R. Collin, Y. Miao, A. Yokochi, P. Enjeti, A. Von Jouanne, Advanced electric vehicle fast-charging technologies, Energies 12 (10) (2019) 1839, doi:10.3390/en12101839.
[2] D. Hall, N. Lutsey, Emerging best pratices for electric vehicle charging infrastructure, White Paper, The International Council on Clean Transportation, Washington, DC, USA, 2017.
[3] T. Donateo, F. Licci, A. D'Elia, G. Colangelo, D. Laforgia, F. Ciancarelli, Evaluation of emissions of CO2 and air pollutants from electric vehicles in Italian cities, Appl. Energy 157 (2015) 675–687, doi:10.1016/j.apenergy.2014.12.089.
[4] E. Ferrero, S. Alessandrini, A. Balanzino, Impact of the electric vehicles on the air pollution from a highway, Appl. Energy 169 (2016) 450–459, doi:10.1016/j.apenergy.2016.01.098.
[5] E.A.M. Falcão, A.C.R. Teixeira, J.R. Sodré, Analysis of CO2 emissions and techno-economic feasibility of an electric commercial vehicle, Appl. Energy 193 (2017) 297–307, doi:10.1016/j.apenergy.2017.02.050.
[6] P. Mock, Z. Yang, Driving electrification: A global comparison of fiscal incentive policy for electric vehicles, White Paper, The International Council on Clean Transportation, Washington, DC, USA, 2014.
[7] S. Loehmann, M. Landau, M. Koerber, A. Butz, Heartbeat: Experience the pulse of an electric vehicle, in: Proc. 6th Int. Conf. Automot. User Interfaces Interact. Veh. Appl., Seattle, WA, USA, Association for Computing Machinery, 2014, pp. 1–10, doi:10.1145/2667317.2667331.
[8] International energy outlookU.S. Energy Information Administration, Office of Energy Analysis, U.S. Department of Energy, Washington, DC, USA, 2019 2019.

[9] J. Dixon, P. Bach, K. Bell, C. Trætholt, On the ease of being green: An investigation of the inconvenience of electric vehicle charging, Appl. Energy 258 (2020) 114090,, doi:10.1016/j.apenergy.2019.114090.
[10] IEEEstandard technical specifications of a DC quick charger for use with electric vehicles, IEEE Standard 2030.1.1-2015, IEEE Vehicular Technology Society, New York, NY, USA, 2016, doi:10.1109/IEEESTD.2016.7400449.
[11] SAEelectric vehicle and plug in hybrid electric vehicle conductive charge coupler, Standard J1772_201710, SAE International, Warrendale, PA, USA, 2017, doi:10.4271/J1772_201710.
[12] Electric vehicle conductive charging system - Part 1General requirements, Standard BS EN IEC 61851-1:2019, The British Standards Institution, 2019.
[13] Electric vehicle conductive charging system - Part 23DC electric vehicle charging station, Standard BS EN IEC 61851-23:2014, The British Standards Institution, 2014.
[14] Connection set for conductive charging of electric vehicles - Part 1General requirements, GB/T 20234.1-2015, National Standard of the People's Republic of China, 2015.
[15] Connection set for conductive charging of electric vehicles - Part 2AC charging coupler, GB/T 20234.2-2015, National Standard of the People's Republic of China, 2015.
[16] Connection set for conductive charging of electric vehicles - Part 3DC charging coupler, GB/T 20234.3-2015, National Standard of the People's Republic of China, 2015.
[17] Electric vehicle conductive charging system - Part 1General requirements, GB/T 18487.1- 2015, National Standard of the People's Republic of China, 2015.
[18] M. Yilmaz, P.T. Krein, Review of battery charger topologies, charging power levels, and infrastructure for plug-in electric and hybrid vehicles, IEEE Trans. Power Electron. 28 (5) (2013) 2151–2169, doi:10.1109/TPEL.2012.2212917.
[19] H.S. Das, M.M. Rahman, S. Li, C.W. Tan, Electric vehicles standards, charging infrastructure, and impact on grid integration: a technological review, Renewable Sustainable Energy Rev 120 (2020) 109618,, doi:10.1016/j.rser.2019.109618.
[20] M. Knez, G.K. Zevnik, M. Obrecht, A review of available chargers for electric vehicles: United States of America, European Union, and Asia, Renewable Sustainable Energy Rev 109 (2019) 284–293, doi:10.1016/j.rser.2019.04.013.
[21] A. Meintz, J. Zhang, R. Vijayagopal, C. Kreutzer, S. Ahmed, I. Bloom, A. Burnham, R.B. Carlson, F. Dias, E.J. Dufek, J. Francfort, K. Hardy, A.N. Jansen, M. Keyser, A. Markel, C. Michelbacher, M. Mohanpurkar, A. Pesaran, D. Scoffield, M. Shirk, T. Stephens, T. Tanim, Enabling fast charging – Vehicle considerations, J. Power Sources 367 (2017) 216–227, doi:10.1016/j.jpowsour.2017.07.093.
[22] N.S. Pearre, W. Kempton, R.L. Guensler, V.V. Elango, Electric vehicles: How much range is required for a day's driving? Transp. Res. Part C Emerging Technol. 19 (6) (2011) 1171–1184, doi:10.1016/j.trc.2010.12.010.
[23] S. Hardman, A. Jenn, G. Tal, J. Axsen, G. Beard, N. Daina, E. Figenbaum, N. Jakobsson, P. Jochem, N. Kinnear, P. Plötz, J. Pontes, N. Refa, F. Sprei, T. Turrentine, B. Witkamp, A review of consumer preferences of and interactions with electric vehicle charging infrastructure, Transp. Res. Part D Transp. Environ. 62 (2018) 508–523, doi:10.1016/j.trd.2018.04.002.
[24] S.A. Funke, F. Sprei, T. Gnann, P. Plötz, How much charging infrastructure do electric vehicles need? A review of the evidence and international comparison, Transp. Res. Part D Transp. Environ. 77 (2019) 224–242, doi:10.1016/j.trd.2019.10.024.
[25] R. Philipsen, T. Brell, W. Brost, T. Eickels, M. Ziefle, Running on empty – Users' charging behavior of electric vehicles versus traditional refueling, Transp. Res. Part F Traffic Psychol. Behav. 59 (2018) 475–492, doi:10.1016/j.trf.2018.09.024.
[26] M. Muratori, E. Kontou, J. Eichman, Electricity rates for electric vehicle direct current fast charging in the United States, Renewable Sustainable Energy Rev 113 (2019) 109235,, doi:10.1016/j.rser.2019.06.042.
[27] R.J. Flores, B.P. Shaffer, J. Brouwer, Electricity costs for an electric vehicle fueling station with Level 3 charging, Appl. Energy 169 (2016) 813–830, doi:10.1016/j.apenergy.2016.02.071.
[28] Y.S. Woo, C.H. Van Dyke, J. Mardall, C. Newport, J.W. Ferguson, Cooling of charging cable, United States Patent, 2016 US 9321362 B2.
[29] C.K. Dyer, M.L. Epstein, D. Culver, Rapid charging electric vehicle and method and apparatus for rapid charging, United States Patent, 2017 US 9786961 B2.
[30] G.T. Mark, Actively cooled electrical connection, United States Patent, 2016 US 9287646 B2.
[31] I. Mudawar, Assessment of high-heat-flux thermal management schemes, IEEE Trans. Compon. Packag. Technol. 24 (2) (2001) 122–141, doi:10.1109/6144.926375.
[32] S.W. Chi, Heat Pipe Theory and Practice: A Sourcebook, Hemisphere Publishing Corp., Washington, DC, USA, 1976.
[33] T.J. LaClair, I. Mudawar, Thermal transients in a capillary evaporator prior to the initiation of boiling, Int. J. Heat Mass Transfer 43 (21) (2000) 3937–3952, doi:10.1016/S0017-9310(00)00042-9.
[34] D. Japikse, Advances in thermosyphon technology, Adv. Heat Transfer 9 (1973) 1–111, doi:10.1016/S0065-2717(08)70061-3.
[35] I. Mudawar, T.M. Anderson, Parametric investigation into the effects of pressure, subcooling, surface augmentation and choice of coolant on pool boiling in the design of cooling systems for high-power-density electronic chips, J. Electron. Packag. 112 (4) (1990) 375–382, doi:10.1115/1.2904392.
[36] J.A. Shmerler, I. Mudawwar, Local heat transfer coefficient in wavy free-falling turbulent liquid films undergoing uniform sensible heating, Int. J. Heat Mass Transfer 31 (1) (1988) 67–77, doi:10.1016/0017-9310(88)90223-2.
[37] A.A. Alhusseini, K. Tuzla, J.C. Chen, Falling film evaporation of single component liquids, Int. J. Heat Mass Transfer 41 (12) (1998) 1623–1632, doi:10.1016/S0017-9310(97)00308-6.
[38] S. Lee, V.S. Devahdhanush, I. Mudawar, Pressure drop characteristics of large length-to-diameter two-phase micro-channel heat sinks, Int. J. Heat Mass Transfer 115 (2017) 1258–1275, doi:10.1016/j.ijheatmasstransfer.2017.08.104.
[39] S. Lee, V.S. Devahdhanush, I. Mudawar, Investigation of subcooled and saturated boiling heat transfer mechanisms, instabilities, and transient flow regime maps for large length-to-diameter ratio micro-channel heat sinks, Int. J. Heat Mass Transfer 123 (2018) 172–191, doi:10.1016/j.ijheatmasstransfer.2018.02.020.
[40] J. Lee, I. Mudawar, Fluid flow and heat transfer characteristics of low temperature two-phase micro-channel heat sinks - Part 1: Experimental methods and flow visualization results, Int. J. Heat Mass Transfer 51 (17–18) (2008) 4315–4326, doi:10.1016/j.ijheatmasstransfer.2008.02.012.
[41] J. Lee, I. Mudawar, Fluid flow and heat transfer characteristics of low temperature two-phase micro-channel heat sinks - Part 2. Subcooled boiling pressure drop and heat transfer, Int. J. Heat Mass Transfer 51 (17–18) (2008) 4327–4341, doi:10.1016/j.ijheatmasstransfer.2008.02.013.
[42] S. Lee, V.S. Devahdhanush, I. Mudawar, Frequency analysis of pressure oscillations in large length-to-diameter two-phase micro-channel heat sinks, Int. J. Heat Mass Transfer 116 (2018) 273–291, doi:10.1016/j.ijheatmasstransfer.2017.08.107.
[43] R.W. Murphy, A.E. Bergles, Subcooled flow boiling of fluorocarbons, Report no. DSR 71903-72, Heat Transfer Laboratory, Department of Mechanical Engineering, Massachusetts Institute of Technology, Cambridge, MA, USA, 1971.
[44] D.C. Wadsworth, I. Mudawar, Enhancement of single-phase heat transfer and critical heat flux from an ultra-high-flux simulated microelectronic heat source to a rectangular impinging jet of dielectric liquid, J. Heat Transfer 114 (3) (1992) 764–768, doi:10.1115/1.2911348.
[45] M.E. Johns, I. Mudawar, An ultra-high power two-phase jet-impingement avionic clamshell module, J. Electron. Packag. 118 (4) (1996) 264–270, doi:10.1115/1.2792162.
[46] W.P. Klinzing, J.C. Rozzi, I. Mudawar, Film and transition boiling correlations for quenching of hot surfaces with water sprays, J. Heat Treat. 9 (2) (1992) 91–103, doi:10.1007/BF02833145.
[47] J.R. Rybicki, I. Mudawar, Single-phase and two-phase cooling characteristics of upward-facing and downward-facing sprays, Int. J. Heat Mass Transfer 49 (1–2) (2006) 5–16, doi:10.1016/j.ijheatmasstransfer.2005.07.040.
[48] M.K. Sung, I. Mudawar, Single-phase and two-phase heat transfer characteristics of low temperature hybrid micro-channel/micro-jet impingement cooling module, Int. J. Heat Mass Transfer 51 (15–16) (2008) 3882–3895, doi:10.1016/j.ijheatmasstransfer.2007.12.016.
[49] A.E. Bergles, W.M. Rohsenow, The determination of forced-convection surface-boiling heat transfer, J. Heat Transfer 86 (3) (1964) 365–372, doi:10.1115/1.3688697.
[50] J.R.S. Thom, W.M. Walker, T.A. Fallon, G.F.S. Reising, Boiling in sub-cooled water during flow up heated tubes or annuli, Proc. Inst. Mech. Eng. 180 (3C) (1965) 226–246, doi:10.1243/PIME_CONF_1965_180_117_02.
[51] J. Shaw, Subcooled boiling heat transfer to liquids under conditions of forced convection PhD Thesis, Chemical Engineering, University of Surrey, Guildford, Surrey, UK, 1972.
[52] H. Muller-Steinhagen, A.P. Watkinson, N. Epstein, Subcooled-boiling and convective heat transfer to heptane flowing inside an annulus and past a coiled wire: Part I—Experimental results, J. Heat Transfer 108 (4) (1986) 922–927, doi:10.1115/1.3247035.
[53] A. Hasan, R.P. Roy, S.P. Kalra, Experiments on subcooled flow boiling heat transfer in a vertical annular channel, Int. J. Heat Mass Transfer 33 (10) (1990) 2285–2293, doi:10.1016/0017-9310(90)90127-G.
[54] N. Kattan, J.R. Thome, D. Favrat, Convective boiling and two-phase flow patterns in an annulus, in: Atti Del X Congresso Nazionale Sulla Transmissione Del Calore, Università degli Studi di Genova, Genoa, Italy, 1992, pp. 309–320.
[55] J.G. Collier, J.R. Thome, Convective Boiling and Condensation, 3rd ed., Clarendon Press, Oxford, UK, 1994, pp. 183–248.
[56] R.W. Bowring, Physical model, based on bubble detachment, and calculation of steam voidage in the subcooled region of a heated channel, HPR-10, Institutt for Atomenergi, OECD Halden Reactor Project, Halden, Norway, 1962.
[57] Y.Y. Hsu, R.W. Graham, An analytical and experimental study of the thermal boundary layer and ebullition cycle in nucleate boiling, Technical Note D-594, Lewis Research Center, NASA, Cleveland, Ohio, USA, 1961.
[58] Y.Y. Hsu, On the size range of active nucleation cavities on a heating surface, J. Heat Transfer 84 (3) (1962) 207–213, doi:10.1115/1.3684339.
[59] T. Sato, H. Matsumura, On the conditions of incipient subcooled-boiling with forced convection, Bull. JSME 7 (26) (1964) 392–398, doi:10.1299/jsme1958.7.392.
[60] E.J. Davis, G.H. Anderson, The incipience of nucleate boiling in forced convection flow, AIChE J. 12 (4) (1966) 774–780, doi:10.1002/aic.690120426.
[61] W.M. Rohsenow, Heat transfer with evaporation, in: Heat Transfer - A Symposium Held at the University of Michigan during the Summer of 1952, University of Michigan Press, 1953, pp. 101–150.
[62] M.M. Shah, A general correlation for heat transfer during subcooled boiling in pipes and annuli, ASHRAE Trans. 83 (1) (1977) 202–217.
[63] P. Saha, N. Zuber, Point of net vapor generation and vapor void fraction in subcooled boiling, in: Proc. Int. Heat Transfer Conf. 5, Tokyo, Japan, Begell House Inc., 1974, pp. 175–179, doi:10.1615/IHTC5.430.

[64] M.M. Shah, New correlation for heat transfer during subcooled boiling in plain channels and annuli, Int. J. Therm. Sci. 112 (2017) 358–370, doi:10.1016/j.ijthermalsci.2016.10.016.
[65] H. Dorra, S.C. Lee, S.G. Bankoff, A critical review of predictive models for the onset of significant void in forced-convection subcooled boiling, Savannah River Technology Center, Westinghouse Savannah River Corporation, Aiken, SC, USA, 1993 WSRC-TR-93-404.
[66] R.E. Lundberg, W.C. Reynolds, W.M. Kays, Heat transfer with laminar flow in concentric annuli with constant and variable wall temperature with heat flux, NASA Technical Note D-1972, Washington, DC, USA, 1963.
[67] W.M. Rohsenow, J.P. Hartnett, Y.I. Cho, Handbook of Heat Transfer, 3rd ed., McGraw-Hill Inc., New York, NY, USA, 1998.
[68] M.M. Shah, Generalized prediction of heat transfer during subcooled boiling in annuli, Heat Transfer Eng. 4 (1) (1983) 24–31, doi:10.1080/01457638108939592.
[69] K.E. Gungor, R.H.S. Winterton, A general correlation for flow boiling in tubes and annuli, Int. J. Heat Mass Transfer 29 (3) (1986) 351–358, doi:10.1016/0017-9310(86)90205-X.
[70] K.E. Gungor, R.H.S. Winterton, Simplified general correlation for saturated flow boiling and comparisons of correlations with data, Chem. Eng. Res. Des. 65 (2) (1987) 148–156.
[71] Z. Liu, R.H.S. Winterton, A general correlation for saturated and subcooled flow boiling in tubes and annuli, based on a nucleate pool boiling equation, Int. J. Heat Mass Transfer 34 (11) (1991) 2759–2766, doi:10.1016/0017-9310(91)90234-6.
[72] G. Zhu, Q. Bi, J. Yan, H. Lv, Experimental study of subcooled flow boiling heat transfer of water in a circular channel under one-side heating conditions, Int. J. Heat Mass Transfer 119 (2018) 484–495, doi:10.1016/j.ijheatmasstransfer.2017.11.111.
[73] S.S. Papell, Subcooled boiling heat transfer under forced convection in a heated tube, NASA Technical Note D-1583, Lewis Research Center, Cleveland, OH, USA, 1963.
[74] M. Badiuzzaman, Correlation of subcooled boiling data, Pak. Eng. 7 (1967) 759–764.
[75] F.D. Moles, J.F.G. Shaw, Boiling heat transfer to sub-cooled liquids under conditions of forced convection, Trans. Inst. Chem. Eng. 50 (1) (1972) 76–84.
[76] F.W. Dittus, L.M.K. Boelter, Heat transfer in automobile radiators of the tubular type, Int. Commun. Heat Mass Transfer 12 (1) (1985) 3–22, doi:10.1016/0735-1933(85)90003-X.
[77] R.H.S. Winterton, Where did the Dittus and Boelter equation come from? Int. J. Heat Mass Transfer 41 (4–5) (1998) 809–810, doi:10.1016/S0017-9310(97)00177-4.
[78] E.N. Sieder, G.E. Tate, Heat transfer and pressure drop of liquids in tubes, Ind. Eng. Chem. 28 (12) (1936) 1429–1435, doi:10.1021/ie50324a027.
[79] J.C. Chen, Correlation for boiling heat transfer to saturated fluids in convective flow, Ind. Eng. Chem. Process Des. Dev. 5 (3) (1966) 322–329, doi:10.1021/i260019a023.
[80] V. Prodanovic, D. Fraser, M. Salcudean, On the transition from partial to fully developed subcooled flow boiling, Int. J. Heat Mass Transfer 45 (24) (2002) 4727–4738, doi:10.1016/S0017-9310(02)00197-7.
[81] P.K. Baburajan, G.S. Bisht, S.K. Gupta, S.V. Prabhu, Measurement of subcooled boiling pressure drop and local heat transfer coefficient in horizontal tube under LPLF conditions, Nucl. Eng. Des. 255 (2013) 169–179, doi:10.1016/j.nucengdes.2012.10.012.
[82] J. Yan, Q. Bi, Z. Liu, G. Zhu, L. Cai, Subcooled flow boiling heat transfer of water in a circular tube under high heat fluxes and high mass fluxes, Fusion Eng. Des. 100 (2015) 406–418, doi:10.1016/j.fusengdes.2015.07.007.
[83] A.P. Colburn, A method of correlating forced convection heat-transfer data and a comparison with fluid friction, Int. J. Heat Mass Transfer 7 (12) (1964) 1359–1384, doi:10.1016/0017-9310(64)90125-5.
[84] M.G. Cooper, Saturation nucleate pool boiling - a simple correlation, in: First UK Natl. Conf. Heat Transfer, IChemE Symp. Ser. 2.86, IChemE, Woodhouse, Leeds, UK, 1984, pp. 785–793, doi:10.1016/b978-0-85295-175-0.50013-8.

Web References

https://www.tesla.com/blog/introducing-v3-supercharging (accessed 11 December 2019).
https://www.ittcannon.com/Core/medialibrary/ITTCannon/website/Literature/Catalogs-Brochures/ITT-Cannon-EVC-DC-Liquid-Cooled-Brochure.pdf (accessed 11 December 2019).
https://www.hubersuhner.com/en/solutions/automotive/products/high-power-charging/radox-hpc-high-power-charging-system (accessed 11 December 2019).
https://assets-us-01.kc-usercontent.com/7de23642-b81e-4adc-808b-d48012b8c326/1df8deea-703c-4908-b4cd-c0cc63bc579f/TRI105.DTA.002_350kW_Veefil-PK%20Data%20Sheet.pdf (accessed 11 December 2019).
https://ionity.eu/en/design-and-tech.html (Accessed 11 December 2019).
https://new.abb.com/news/detail/5227/abb-chargers-power-ionitys-opening-of-europes-highway-of-the-future (accessed 11 December 2019).
https://search-ext.abb.com/library/Download.aspx?DocumentID=4EVC700601-LFUS&LanguageCode=en&DocumentPartId=&Action=Launch (Accessed 11 December 2019).
http://www.btcpower.com/doc/350kW-DCFC.pdf (Accessed 11 December 2019).
https://electricmobility.efacec.com/wp-content/uploads/2018/03/CS332I1606F1_HV.pdf (Accessed 11 December 2019).
https://www.chargepoint.com/files/en-gb/datasheets/ds-expressplus.pdf (Accessed 12 December 2019).
https://new.siemens.com/global/en/products/mobility/road-solutions/electromobility/ecars-high-power-charging-infrastructure.html (Accessed 12 December 2019).
https://www.evgo.com/about/news/evgo-abb-deploy-nations-first-high-power-electric-vehicle-fast-charging-station/ (Accessed 12 December 2019).
http://telluspower.com/wp-content/uploads/2015/05/DC-200KW-Tellus-Power-TP-EVPD-GBT-750200CGY2-india.pdf (Accessed 12 December 2019).
https://www.dbt.fr/en/our-products/dispenser/ (Accessed 12 December 2019).
https://www.endesa.com/en/press/news/d201911-endesa-and-tmb-install-2-new-pantographs-to-charge-electric-buses-in-barcelona.html (Accessed 12 December 2019).
https://circontrol.com/wp-content/uploads/2019/11/Circontrol-Raption150.pdf (Accessed 12 December 2019).
https://www.phihong.com/admin/uploads/DO360.pdf (Accessed 12 December 2019).
https://info.freewiretech.com/hubfs/FreeWire_Boost_Charger_datasheet.pdf (Accessed 12 December 2019).